

國立交通大學

光電工程研究所

博士論文

發光二極體於功能性頻譜照明之研究

An investigation into functional spectral illumination
with LED white composite spectra

研究生：簡銘進

指導教授：田仲豪教授

中華民國 一百零一年 七月

發光二極體於功能性頻譜照明之研究

An investigation into functional spectral illumination
with LED white composite spectra

研究生：簡銘進

Student : Ming-Chin Chien

指導教授：田仲豪

Advisor : Dr. Chung-Hao Tien

國立交通大學 電機學院

光電工程研究所

博士論文

A Thesis

Submitted to Institute of Electro-Optical Engineering
College of Electrical Engineering and Computer Science

National Chiao-Tung University

in Partial Fulfillment of the Requirements

for the Degree of Doctor of Philosophy

in

Electro-Optical Engineering

July 2012

Hsin-Chu, Taiwan, Republic of China

中華民國 一百零一年 七月

發光二極體於功能性頻譜照明之研究

博士研究生：簡銘進

指導教授：田仲豪教授

國立交通大學
光電工程研究所

摘 要

隨著近年發光二極體(Light emitting diode, LED)的快速發展，多種 LED 頻譜組合的 LED 系統已充分具有應用潛能，可根據不同操作目的策略性的調制其複合頻譜能量分布。以一般照明為例，對於一目標色溫，LED 系統可藉由頻譜調制提升整體效率與演色性，並拓展適用的環境溫度範圍。延伸到智能照明，則可根據使用者對照明色溫變化的需求調整到對應的頻譜，同時維持系統高效能運作。在醫療照明上的應用，需要更著重於頻譜在溫度與電流變化下的可預測性。

然而，一般而言高功率單色光或螢光轉換的 LED，其 SPD 的變化相對於界面溫度與驅動電流為非線性的關係，因而增加了系統頻譜優化的困難度，導致上述的應用目標難以達成。本論文基於目前市面上商用的 LED 元件，以現有的製程與材料為基礎，針對各終端應用發展一種 LED 頻譜調制最佳化的解決方案，建立精確頻譜模型與完整的優化設計流程。

本論文提出將一般非完全對稱的 LED 頻譜分解成雙高斯函數，準確的預測 LED 頻譜在不同溫度與電流下的行為，並將此模型推展到螢光粉轉換白光 LED (phosphor-converted white LED)。

本論文並嘗試以不同角度切入，成功引入透鏡幾何光學系統設計的概念，針對複合 LED 照明系統 SPD 提出相對應的完整設計流程：(1) 初始系統，(2) 邊界條件，(3) 優化，(4) 價值函數分析，(5) 判斷，與 (6) 容忍度分析。最終以此技術分別應用於低功率與高功率 LED 照明系統，實現色溫可調、適用環境溫度廣泛、演色性佳的高效率照明設計。

An investigation into functional spectral illumination with LED white composite spectra

Doctoral Student: Ming-Chin Chien Advisor: Dr. Chung-Hao Tien

**Institute of Electro-Optical Engineering
National Chiao Tung University**

Abstract

With the rapid progress in light-emitting diode techniques, all kinds of lighting purposes can be achieved by strategically manipulating the spectral power distributions of LEDs clusters. For example, in general lighting there is a fundamental tradeoff between the efficiency and color rendering quality, where an optimal boundary (the Pareto Front) will be produced. By optimizing the composite spectrum, the LEDs lighting system can be operated alongside the boundary. When the spectral-controllable technique is utilized to fields of intelligent illumination, the color temperature can be adjusted in accordance with end demands. As to the medical lighting, the spectral distortion will be predictable with respect to variant ambient temperature and drive current.

In this dissertation, a novel methodology for spectral manipulation has been proposed, including a well-defined spectral model and six optimization steps. The spectral model employing the double-Gaussian function can closely estimate the practical spectrum that is imperfectly symmetric and depends on the junction temperature. For the optimization, the concept in imaging system design has successfully been adopted to develop a composite spectral process. The proposed algorithm would be applied to the low power and high power cluster, respectively, to

achieve the color-tunable systems with high efficiency, high color rendering property as well as wide operation window at ambient temperature.



誌 謝

一轉眼，加入田仲豪老師的研究群已經八年了。一路走來，有許多的點滴在心頭；在這些年的研究當中，要感謝的人真的很多，僅以此文表達我的誠摯謝意。

我衷心的感謝田仲豪老師在研究上、表達能力上、甚至生活細節上的悉心指導，並提供十分優良的研究環境，讓我有許多的機會到國內外的企業或是研究單位實習，並參加國際級的研討會以開闊我的視野。也由衷的感謝Stefan Sinzinger教授在Ilmenau半年的細心照顧與指導，且在我回國後更仍不斷的關心與鼓勵我。能成為田老師與Sinzinger教授的指導學生，實在是我畢生的福氣且著實讓我受益良多，因此方能順利地完成本篇論文。此外，也感謝各位口試委員所提供的寶貴意見，使本論文更加的完備。

在這些年的研究生生活中，要感謝李企桓學長、鄭裕國學長、鄭榮安學長與鄭璧如學姊對我的引領與幫忙，也感謝一同奮鬥的小陸、健翔與Blue，和你們一起的相互討論與扶持，是研究生生活裡很大的助益。另外，這些年來一同工作過的學弟妹們，貢丸、松柏、董哥、志宏、玉麟、及筱儒，謝謝你們的協助，也給了我許多與你們一同學習的機會。而對於許多已經畢業的優秀碩士班學弟妹們，以及目前在這個實驗室繼續奮鬥的同儕們，謝謝你們一同經營了這個溫馨且愉快的研究環境，還要謝謝最照顧我的助理古明嫻小姐以及其他美麗的助理小姐們，讓我八年來的研究生生活充滿了無限的回憶。

在Technische Universität Ilmenau研究的期間，感謝Matthias、Jürgen、Karolin、馬玄與欣育的照顧，讓我少吃很多的苦頭，也謝謝Sinzinger教授實驗室其他幫忙我的好朋友們，讓我在德國半年期間度過了非常美好的時光。

此外，在沛鑫半導體實習的日子，要感謝陳志隆教授與韋安琪學姊的指導，使我對於光學設計在實作上有更進一步的認識，也感謝玉樹、育佳及小小，還有許多曾經幫助過我的人，謝謝你們的協助。

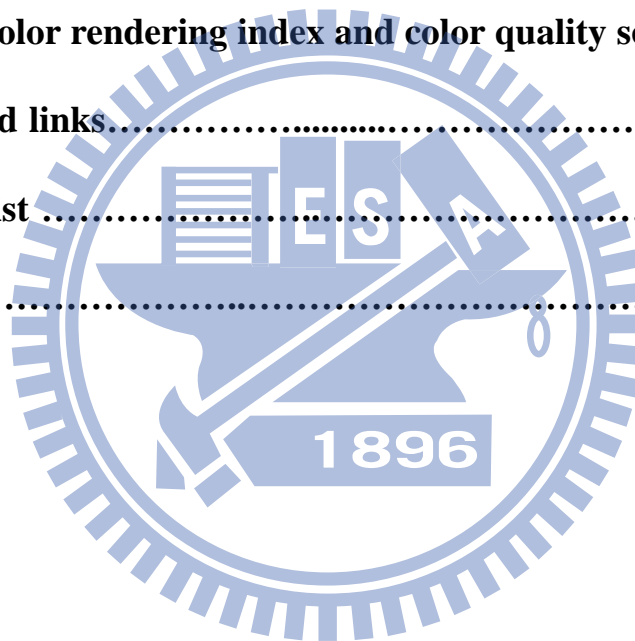
對於我最親愛的父母親，真的謝謝你們三十年來對我的支持與鼓勵，讓我變得更有自信且成熟穩重，如今我即將邁入人生的另一個階段，在未來的日子裡我必當竭盡所能來報答你們、孝順你們。而在這些日子裡，真的很感謝陪伴著我的筱儒，在我最低潮的時候有妳陪我一起渡過，最開心的時候有妳跟我一起分享；謝謝我的家人對我所付出的一切，讓我在此致上我最誠摯的感謝。

Contents

Abstract (Chinese)	i
Abstract (English)	ii
Contents	v
List of Figures	viii
List of Tables	xi
List of Symbols	xii
1 Introduction	1
1.1 Additive mixing	2
1.1.1 Simplified mixing condition	2
1.1.2 Ideal trichromatic color mixing scheme	4
1.2 Thermal and current dependences of LEDs spectra	7
1.2.1 Prior arts in consideration of thermal and current issues	8
1.3 Ideal multispectral mixing optimization	9
1.4 Aspects regarding the practical realization of LEDs cluster.....	11
1.4.1 Spectral characteristic	11
1.4.2 Color quality index	11
1.4.3 Energy evaluation	12
1.5 Motivation and objective of this thesis	12
1.6 Organization of this thesis.....	14
2 LED Spectral Characterization	16
2.0 Goal.....	16
2.1 Junction temperature measurement.....	17
2.1.1 Forward voltage method	17
2.1.2 Junction temperature estimation	18
2.2 Junction temperature determination.....	22
2.3 LED spectral modeling	25
2.3.1 Double Gaussian model	25
2.3.2 Single-colour spectral function	26

2.3.3 Phosphor-converted spectral function	29
2.4 Validation of the spectral model	30
2.5 Summary and conclusions	32
3 Multispectral Mixing Optimization as Lens Design Techniques	34
3.0 Goal.....	34
3.1 Initial system.....	36
3.2 Define boundary conditions.....	38
3.3 Optimization	39
3.3.1 Metamerism	39
3.3.2 Continous genetic alogrithm.....	42
3.4 Merit analysis.....	45
3.4.1 Merit function and Pareto front	45
3.4.2 Sampling method SA_1	46
3.4.3 Sampling method SA_2	48
3.5 Judgment.....	49
3.6 Tolerance analysis.....	50
3.7 Summary and conclusions	51
4 Applications of the Multispectral Mixing Scheme	52
4.0 Goal.....	52
4.1 Case 1: Low power LEDs cluster design.....	53
4.1.1 Validation of the composite spectrum.....	54
4.1.2 Comparison of R/G/B and R/G/B/A system	55
4.1.3 The effect of cool-white LED	57
4.1.4 The color tunable R/G/B/A/CW system	59
4.2 Case 2: High power LEDs cluster design	59
4.2.1 The influence of ambient temperature on color mixing.....	60
4.2.2 Spectral modulation with thermal compensation.....	62
4.2.3 Optimized pentachromatic LEDs cluster	65
4.3 Summary and conclusions	66

5	Conclusions and Future Works	68
5.1	Conclusions.....	68
5.1.1	LED Spectral Characterization	68
5.1.2	Multispectral Optimization as Lens Design Techniques.....	69
5.1.3	Applications of the Multispectral Mixing Scheme	70
5.2	Future works	71
5.2.1	Other applications	71
5.2.2	Reverse model.....	73
5.2.3	Summary	76
	Appendix – Color rendering index and color quality scale.....	77
	References and links.....	80
	Publication List	84
	Vita	86



List of Figures

1-1.	The schematic interaction between light sources, objects, and detectors	2
1-2.	CIE 1931 and CIE 1978 \bar{x} \bar{y} \bar{z} color matching functions. The CIE 1931 version is the currently valid official standard ^[3]	3
1-3.	Principle of color mixing illustrated by three emission lines with chromaticity coordinates (x_1, y_1) , (x_2, y_2) , and (x_3, y_3) . The mixed color has the coordinate (x, y)	6
1-4.	The spectrum of phosphor-converted white LED changes with respect to ambient temperature T_a	7
1-5.	Conceptual analogy between the <i>SPD</i> synthesis and conventional lens design. A LED cluster composed of red/cool-white/cool-white/green (R/CW/CW/G) can be regarded as a double Gauss lens system with two singlet lenses and two cemented doublets, where the cool-white LED is caused by dichromatic mixing	14
2-1.	Typical semi-log current-voltage characteristic of a green InGaN LED (HELIO Optoelectronics Corp., HMHP-E1HG)	19
2-2.	The voltage-temperature characteristic of a green InGaN LED (HELIO Optoelectronics Corp., HMHP-E1HG) at five current levels	20
2-3.	The distribution of all elements in Gaussian power \mathbf{p} and its fitting coefficient values c_{p1} , c_{p2} and c_{p3} for the red AlInGaP LED	28
2-4.	The deviation and goodness of fit for Gaussian power distribution fitting For the red AlInGaP LED	28
2-5.	The illustration of the simulation model and the experimental measurement for green and phosphor LED spectra at $T_j = 25$ °C and $I_{DC} = 350$ mA, respectively	30
3-1.	Design procedure of (a) lens design and (b) spectral synthesis of a LED cluster. Both flow charts include six steps: (3.1) initial system, (3.2) define boundary condition, (3.3) optimization, (3.4) aberration or merit analysis, (3.5) judgment, and (3.6) tolerance analysis.....	35

3-2.	Normalized luminous efficiency of visible LED made from GaInN and AlGaInP series versus individual peak wavelength. The LED with high LE is analogous to the lens with high refractive index.....	36
3-3.	Schematic process of the continuous genetic algorithm (CGA).....	42
3-4.	(a) The illustration of the Pareto fronts PF_s for different CT_s on the $CQS - LE$ plane. (b) The flowchart of SA_1 . Either end point P_0 or P_1 located within quadrant III will lead to an unacceptable performance as PF_3 . The curve with end points located within quadrant II and IV, like PF_2 , should be confirmed the operation portion (red curve)	47
3-5.	A green wavelength inserted at the large wavelength interval.....	49
3-6.	Two or more single-colour spectrum replaced by a phosphor- converted source	49
3-7.	An operating wavelength of too-high emission split into two adjacent wavelength	50
4-1.	The spectra of red (R), green (G), blue (B), amber (A) and cool-white (CW) LEDs at ambient temperature T_a of 25 °C with all drive currents of 20 mA. The corresponded chromaticity points and specifications are also shown in the figure. The drive currents controlled by PWM approach have the pulse width of 6.66 ms at differences of 0.04 ~ 0.06 ms for each gray level (a total of 128 gray levels)	53
4-2.	Spectral comparisons of simulations and experiments for P_0 and P_1 at CT_s of 6500K and 3000K, respectively. The simulated spectra closely matched the measurements in spite of a few peak deviations.....	54
4-3.	The illuminant environments at (a) P_0 ($CQS = 87$ points, $LE = 66$ lm/watt) for $CT = 6500K$ and (b) P_0 ($CQS = 69$ points, $LE = 67$ lm/watt) for $CT = 3000K$ show apparently different color rendering abilities.....	55
4-4.	The SA_2 results of (a) R/G/B (black curve), R/G/B/A, and (b) R/G/B/A/CW clusters aimed to P_1 and P_0 for full range of CT from 1000K to 10000K.....	56
4-5.	The results of $CQS_{1/0}$ and $LE_{1/0}$ for R/G/B/A and R/G/B/A/CW clusters. By using	

SA ₂ analysis, R/G/B/A/CW can further extend the operation window in color temperature	57
4-6. (a) The values of <i>CQS</i> and <i>LE</i> , and (b) the stacked emission power ratio versus color temperature for the optimized R/G/B/A/CW design ($CQS_m = 80$ points and $LE_m = 60$ lm/watt). The operation window has been extended to $2600K < CT < 8500K$ with the selected weight via SA ₂ selection method. It is noted that the operation window is mainly restricted by the <i>CQS</i> due to the correction factor at the extreme color temperature	58
4-7. The power spectra of red ($\lambda_R: 625nm, \Delta\lambda_R: 20nm$), green ($\lambda_G: 523nm, \Delta\lambda_G: 33nm$), blue ($\lambda_B: 465nm, \Delta\lambda_B: 25nm$), amber ($\lambda_A: 587nm, \Delta\lambda_A: 18nm$) and cool-white LEDs at T_a of 10 °C with I_{DC} of 350 mA. The upper right figure shows a real-field test designed for $CT = 5000K$ and the lower right one shows the utilized LEDs attached on the temperature controllable fixture respectively	60
4-8. The temperature dependence of spectra designed for $CT = 3200K, 4600K, 6200K,$ and $7400K$ at $T_a = 50$ °C. The chromaticity point shifts toward higher color temperature with the raise of T_a owing to the dramatic deterioration in <i>LEs</i> of the red and amber LEDs	61
4-9. The temperature dependence of <i>LE</i> for pentachromatic LEDs. When T_a is varied from 10 °C to 100 °C, <i>LEs</i> of amber and red AlInGaP LEDs decrease to 23% and 46% of that at 10 °C while <i>LEs</i> of InGaP LEDs are insensitive to temperature variation	62
4-10. The <i>LE</i> contour of the pentachromatic LEDs cluster is performed under the predefined requirements ($CQS > 85$ points, lighting level =100 lm and $\Delta xy < 0.01$). When the $LE = 100$ lm/watt is selected as the minimum efficiency boundary, a full operation range for ambient temperature can be obtained for $CT > 5200K$	66
5-1. Configuration of the spectral tunable system.....	73
5-2. The schematic process of the reverse model.....	74
A-1. <i>CRI</i> test color samples.....	77
A-2. <i>CQS</i> test color samples	79

List of Tables

2-1. Pentachromatic LEDs, specific pulsed current I_0 , slopes γ and γ' , and intercepts γ and γ' of the linear approximation.....	21
2-2. The values of fitting parameters c , d , e , and f for pentachromatic LEDs at ambient temperature $T_a = 50^\circ\text{C}$	24
2-3. The DC drive current I_{DC} , electrical power P_e , optical power Φ and junction temperature T_j for red AlInGaP LED (HELIO Optoelectronics Corp., HMHP-E1HR) at ambient temperature $T_a = 50^\circ\text{C}$	24
2-4. The parameters of approximated phosphor-converted LED spectrum. The blue and fluorescence components should be individually considered.....	31
2-5. The comparison of the simulation and measurement on luminous flux and CIE colour coordinates for all sample LEDs.....	32
4-1. The comparison of CQS , LE , output spectral power P , correlated color temperature CCT , color temperature CT and the input power ratio P_{in} under $T_a = 10^\circ\text{C}$, 50°C and 100°C	63
A-1. CRI values for common lamps.....	78

List of Symbols

The table below lists the symbols that were used in this thesis for quick reference. In some cases, the use of the same symbol to refer to two different things was inevitable. In such cases, the meaning should be clear from the context

\mathbf{A}	eigenvalue matrix
β	random number within interval [0, 1]
B	Boltzmann constant
c	coefficients, the corresponded weight of point P_c
\mathbf{c}	coefficient vector
\mathbf{C}	coefficient matrix
\mathbf{C}_C	matrix of chromaticity coordinates
\mathbf{C}_M	matrix of color-matching functions
\mathbf{C}_{ov}	covariance matrix
$\hat{\mathbf{C}}_M$	matrix of color-matching functions with values on peak wavelengths
δ	intercept
Δ	small difference
e	elementary charge
\mathbf{E}	eigenvector matrix
\mathbf{E}'	eigenvector matrix with the reduced dimensionality
f	focal length
γ	slope
g	Gaussian function
\mathbf{g}	Gaussian function vector
G	value of merit function
\mathbf{G}	Gaussian function matrix
I	current
I_p	pulsed current
I_s	saturation current
\mathbf{i}_{qu}	quadratic current basis vector
\mathbf{i}_{DC}	DC drive current vector
$\tilde{\mathbf{i}}_{DC}$	magnified DC drive current vector
\mathbf{I}_{DCP}	matrix of initial DC current population
K	total types of LED
λ	wavelength
$\hat{\lambda}$	peak wavelength

$\hat{\lambda}$	peak wavelength vector
$\Delta\lambda$	spectral width
$\Delta\boldsymbol{\lambda}$	spectral width vector
m	number of spectral vector
\mathbf{m}	basis vector
\mathbf{m}_c	vector of mixed light's chromaticity coordinates
M	total number of spectral vector
\mathbf{M}	basis matrix
n	refractive index, number of sampling wavelength, number of population
n_{ideal}	ideality factor
N	total number of sampling wavelength
\mathbf{O}	matrix operator
ϕ	optical lens power
Φ	radiant flux
Φ_v	luminous flux
P	power of Gaussian function
\mathbf{P}	Gaussian power vector
P_e	electric power
P_{in}	electric power ratio
\mathbf{P}	principal component
r	surface curvature
R	radius of the lens surface
R_j	thermal resistance between junction and reference point
\mathbf{s}	spectral function vector
$\tilde{\mathbf{s}}$	vector of estimated spectral function
S	spectral function
S_m	mean value of the spectral function
\tilde{S}	estimated spectral function
\tilde{S}_m	mean value of the estimated spectral function
\mathbf{S}	spectral function matrix
$\tilde{\mathbf{S}}$	matrix of estimated spectral function
$\tilde{\mathbf{S}}_p$	matrix of estimated spectral population
\mathbf{t}	vector of target tristimulus values
$\tilde{\mathbf{t}}$	vector of current tristimulus values
\mathbf{t}_j	junction temperature vector
T_a	ambient temperature
T_j	junction temperature
\mathbf{T}	transformation matrix

\mathbf{T}_{jp}	matrix of junction temperature population
V	photopic eye sensitivity function
V_{DC}	DC forward voltage
V_f	forward voltage
w	weight
\mathbf{w}	weight vector
x	chromaticity coordinate
\bar{x}	color matching function of CIE 1931 \bar{x} \bar{y} \bar{z}
X	CIE 1931 XYZ tristimulus value
y	chromaticity coordinate
\bar{y}	color matching function of CIE 1931 \bar{x} \bar{y} \bar{z}
Y	CIE 1931 XYZ tristimulus value
\bar{z}	color matching function of CIE 1931 \bar{x} \bar{y} \bar{z}
Z	CIE 1931 XYZ tristimulus value



Chapter 1

Introduction

The progress in Light-emitting diodes (LEDs) technology has been breathtaking during the last few decades. At this time, great technological advances in LEDs are profoundly changing the way light was generated. In contrast to many conventional light sources, LEDs not only have the potential of converting electricity to light with near-unit efficiency, but also offer impressive controllability of their spatial distribution, temporal modulation, and polarization property ^{[1]-[4]}. With an arrangement of multispectral LEDs, the LEDs cluster could particularly have the capability of manipulating its synthesized spectral power distributions (*SPDs*). Such intelligent light sources could be adjusted according to different operational environments and requirements. As a result, tremendous properties of LEDs or LEDs cluster lead to great benefits across a wide field of applications, including lighting, transportation, communication, imaging, agriculture, and medicine ^{[5]-[8]}. In this doctoral research, we mainly focus on the spectral part of LEDs – in particular, spectral characterization and multispectral mixing methodology. A better understanding of additive mixing will be required to attain good design in practical applications.

1.1 Additive mixing

Figure 1-1 shows a general description of the additive mixing event. Light sources, e.g. LEDs clusters, are quantified by the spectral power distributions (*SPDs*). Objects are specified by the transmitted, reflected, or scattered spectral distributions, which depend on the illuminating and detecting geometrical conditions. The detectors are quantified through the sensor response curves.

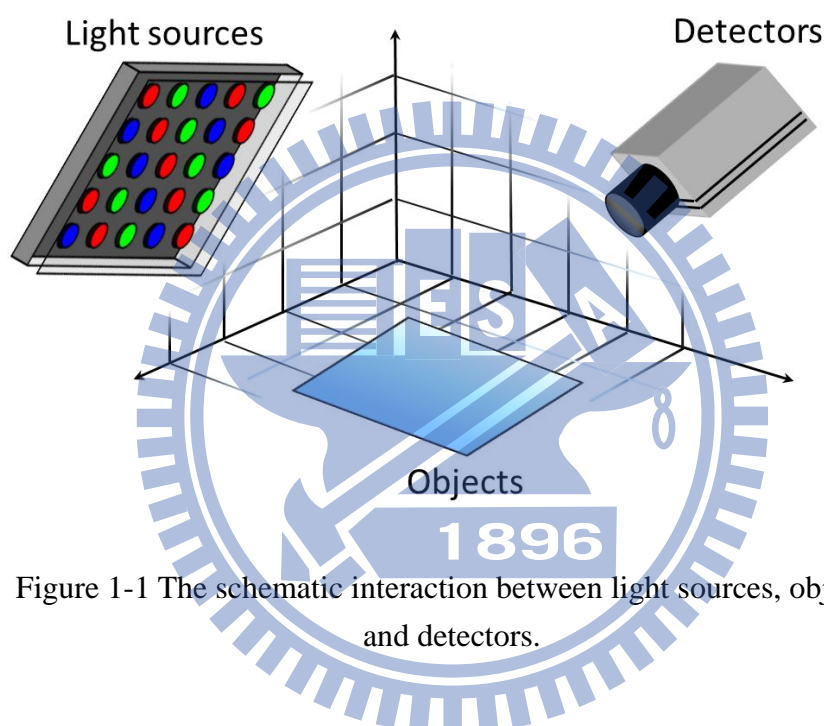


Figure 1-1 The schematic interaction between light sources, objects, and detectors.

1.1.1 Simplified mixing condition

In order to elaborate the principle of additive mixing in a more understandable way, the condition is simplified by several assumptions:

1. Photometric units are used. The light and color sensation are characterized by the human eye. The luminance levels outside of the photopic vision regime and the spectral radiations beyond the human perceptual range are irrelevant when it comes to light perception by a human being. For example, when luminous level $< 0.003 \text{ cd/m}^2$ (scotopic vision regime), such as in a moonless night, objects lose

their colors but only appear to have different gray levels.

2. The influences of objects are eliminated. Objects are ideally regarded as white lambertian surfaces with unit spectral reflectance for all visible wavelengths. Thus the effects of the source-object-detector geometrical conditions on spectral detection are ignorable. The results of additive mixing only depend on the correlation of the synthesized spectral emissions and sensor response curves.

3. The sensor response curves are color-matching functions. *The International Commission for Illumination (Commission Internationale de l'Eclairage, CIE)* standardized the measurement of color by means of three dimensionless quantities, $\bar{x}(\lambda)$, $\bar{y}(\lambda)$, and $\bar{z}(\lambda)$, called color-matching functions. The $\bar{y}(\lambda)$ is identical to the photopic eye sensitivity function $V(\lambda)$ that the CIE introduced for conversion between the radiometric and photometric units. As shown in Figure 1-2, the CIE (1931) color-matching functions reflect the three bases of human color vision. The color of any light source can be indicated by projecting its spectrum on bases, i.e. lengths of three projections, named tristimulus values.

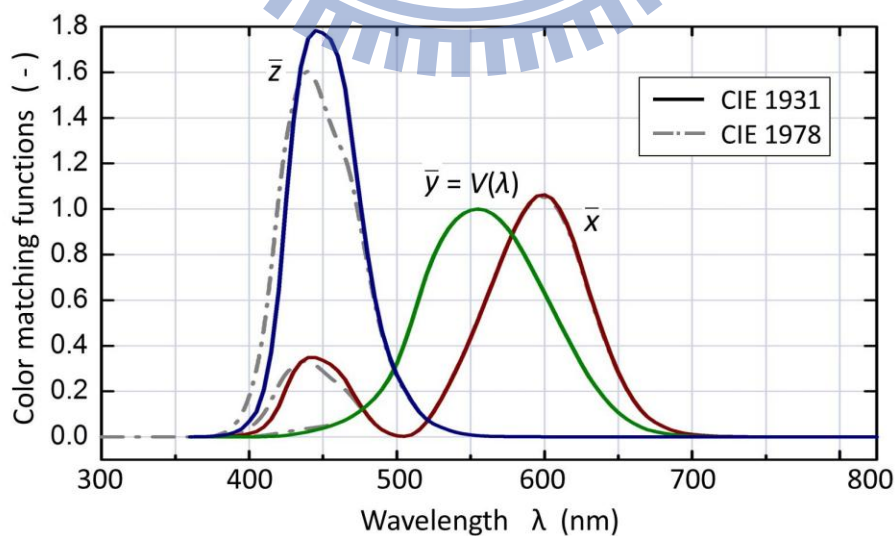


Figure 1-2 CIE 1931 and CIE 1978 \bar{x} \bar{y} \bar{z} color matching functions. The CIE 1931 version is the currently valid official standard ^[9].

4. The number of multispectral light sources is three. Assume that the three emission bands have spectral distribution function $S_1(\lambda)$, $S_2(\lambda)$, and $S_3(\lambda)$, whose bandwidths are much narrower than any of the color-matching functions. We further assume $S_1(\lambda)$, $S_2(\lambda)$, and $S_3(\lambda)$ have scalability and linearity with respect to their drive currents. In addition, the chromaticity coordinates of three light sources (x_1, y_1) , (x_2, y_2) , and (x_3, y_3) are regularly located in the red, green, and blue regions of the chromaticity diagram.

1.1.2 Ideal trichromatic color mixing scheme

Next, we determine tristimulus values X , Y , and Z of the mixed light from the aforementioned assumptions^[10]:

$$\begin{aligned}
 X &= X_1 + X_2 + X_3 \\
 &= \int_{\lambda} \bar{x}(\lambda) S_1(\lambda) d\lambda + \int_{\lambda} \bar{x}(\lambda) S_2(\lambda) d\lambda + \int_{\lambda} \bar{x}(\lambda) S_3(\lambda) d\lambda \\
 &\approx \bar{x}(\hat{\lambda}_1) S_1(\hat{\lambda}_1) + \bar{x}(\hat{\lambda}_2) S_2(\hat{\lambda}_2) + \bar{x}(\hat{\lambda}_3) S_3(\hat{\lambda}_3) \\
 &\approx \bar{x}(\hat{\lambda}_1) c_1 I_{DC1} + \bar{x}(\hat{\lambda}_2) c_2 I_{DC2} + \bar{x}(\hat{\lambda}_3) c_3 I_{DC3}
 \end{aligned} \tag{1-1}$$

$$Y = Y_1 + Y_2 + Y_3 \approx \bar{y}(\hat{\lambda}_1) c_1 I_{DC1} + \bar{y}(\hat{\lambda}_2) c_2 I_{DC2} + \bar{y}(\hat{\lambda}_3) c_3 I_{DC3} \tag{1-2}$$

$$Z = Z_1 + Z_2 + Z_3 \approx \bar{z}(\hat{\lambda}_1) c_1 I_{DC1} + \bar{z}(\hat{\lambda}_2) c_2 I_{DC2} + \bar{z}(\hat{\lambda}_3) c_3 I_{DC3} \tag{1-3}$$

where X_i , Y_i , and Z_i are the tristimulus values of i th emission band. Similarly, $\hat{\lambda}_i$ and I_{DCi} refer to the peak wavelength and the DC drive current of the i th emission band respectively. The factors c_1 , c_2 , and c_3 are the constants, relating drive current I_{DC} to peak value of spectral function $S(\hat{\lambda})$ for each light source. The Equations (1-1) – (1-3) can be expressed by a matrix form:

$$\hat{\mathbf{C}}_{\mathbf{M}} \check{\mathbf{i}}_{\text{DC}} = \check{\mathbf{t}} \quad (1-4a)$$

$$\hat{\mathbf{C}}_{\mathbf{M}} = \begin{bmatrix} \bar{x}(\hat{\lambda}_1) & \bar{x}(\hat{\lambda}_2) & \bar{x}(\hat{\lambda}_3) \\ \bar{y}(\hat{\lambda}_1) & \bar{y}(\hat{\lambda}_2) & \bar{y}(\hat{\lambda}_3) \\ \bar{z}(\hat{\lambda}_1) & \bar{z}(\hat{\lambda}_2) & \bar{z}(\hat{\lambda}_3) \end{bmatrix}, \quad \check{\mathbf{i}}_{\text{DC}} = \begin{bmatrix} \alpha I_{\text{DC1}} \\ \beta I_{\text{DC2}} \\ \gamma I_{\text{DC3}} \end{bmatrix}, \quad \text{and } \check{\mathbf{t}} = \begin{bmatrix} X \\ Y \\ Z \end{bmatrix} \quad (1-4b)$$

Through this paper, vectors are denoted by bold-faced lower-case letters, e.g., $\check{\mathbf{t}}$ (current tristimulus values), $\check{\mathbf{i}}_{\text{DC}}$ (magnified DC drive current). Matrices are represented by bold-faced capital letters, e.g., $\hat{\mathbf{C}}_{\mathbf{M}}$ (peak values of color-matching functions). Equation (1-4) shows the system of trichromatic color mixing is critically determined, i.e. the system operator matrix $\hat{\mathbf{C}}_{\mathbf{M}}$ is square. If we consider an inverse problem, the number of elements in the required vector $\check{\mathbf{t}}$ is equal to the number of components of the unknown vector $\check{\mathbf{i}}_{\text{DC}}$. In this case, solution of the inverse problem is equivalent to finding a matrix operator \mathbf{O} , which satisfies the condition:

$$\mathbf{O}\check{\mathbf{t}} = \check{\mathbf{i}}_{\text{DC}} \quad (1-5)$$

where the expression of $\check{\mathbf{t}}$ can be substituted by Equation (1-4) to yield the consequence:

$$\mathbf{O} = \hat{\mathbf{C}}_{\mathbf{M}}^{-1} \quad (1-6)$$

The existence of inverse matrix $\hat{\mathbf{C}}_{\mathbf{M}}^{-1}$ is based on the condition that row vectors of system matrix $\hat{\mathbf{C}}_{\mathbf{M}}$ are linearly independent. As a result, the DC drive current for each emission band is likely to be obtained.

To further gain the insight of additive color mixing, we calculate the set of chromaticity coordinates of the mixed light $\mathbf{m}_{\mathbf{C}}$ from the linear combination of

chromaticity coordinates of three light sources (x_1, y_1) , (x_2, y_2) , and (x_3, y_3) :

$$\mathbf{C}_c \mathbf{w} = \mathbf{m}_c \quad (1-7a)$$

$$\mathbf{C}_c = \begin{bmatrix} x_1 & x_2 & x_3 \\ y_1 & y_2 & y_3 \end{bmatrix}, \quad \mathbf{w} = \begin{bmatrix} w_1 \\ w_2 \\ w_3 \end{bmatrix}, \quad \text{and} \quad \mathbf{m}_c = \begin{bmatrix} x \\ y \end{bmatrix} \quad (1-7b)$$

where the set of weight factors \mathbf{w} is defined as:

$$\mathbf{w} = \frac{1}{\text{sum}(\mathbf{t})} \hat{\mathbf{C}}_M^T \tilde{\mathbf{i}}_{DC} \quad (1-8)$$

Therefore, the principle of color mixing can be illustrated in Figure 1-3. Three chromaticity points, red, green, and blue, connected by the straight dash line, represent three vertices of the triangle. The area of the triangle, called the color gamut, include all colors that can be linearly synthesized by the three emission bands.

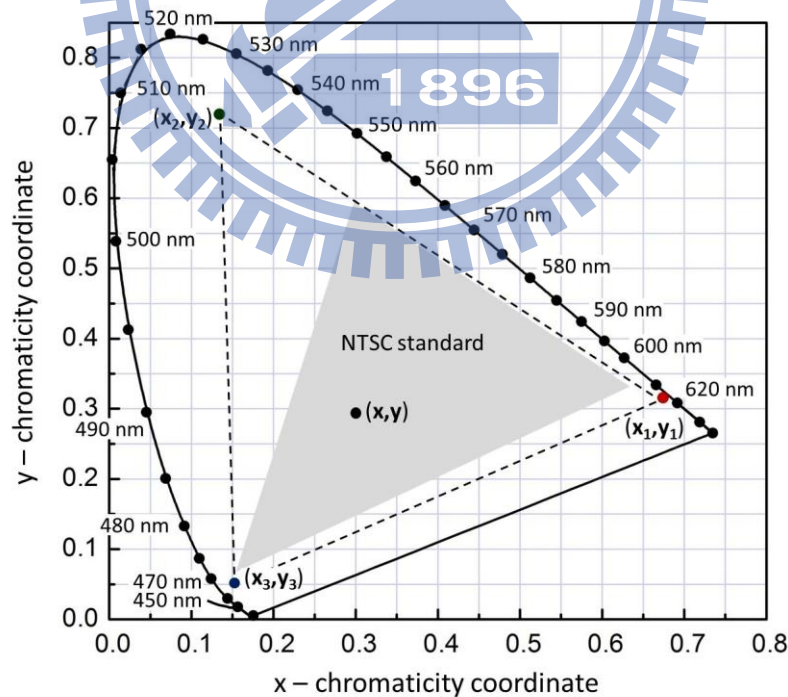


Figure 1-3 Principle of color mixing illustrated by three emission lines with chromaticity coordinates (x_1, y_1) , (x_2, y_2) , and (x_3, y_3) . The mixed color has the coordinate (x, y) .

For the case of dichromatic color mixing, $w_3 = 0$, the color gamut will degenerate to a straight line connecting two end points of two light sources, i.e. the edge of the triangle with end points red and green. Any chromaticity point locate on the line can be linearly combined by the two emission bands.

1.2 Thermal and current dependences of LEDs spectra

In previous section we have considered the narrower spectral widths of sources to simplify mixing mechanism. Furthermore, we assumed emission spectra have scalability and linearity with respect to their drive currents without thermal consideration. As a matter of fact, the spectral widths are thermally broadened, whose full-width at half-maximum $\Delta\lambda$ of $2 kT$ to $10 kT$ have been found experimentally for the GaInN series LEDs at room temperature ($kT = 25.9$ meV at 300 K). The spectral features, i.e. emission power, peak wavelength and spectral width of inorganic LED, vary nonlinearly with junction temperature and drive current. An example of distorted white light spectrum is illustrated in Figure 1-4.

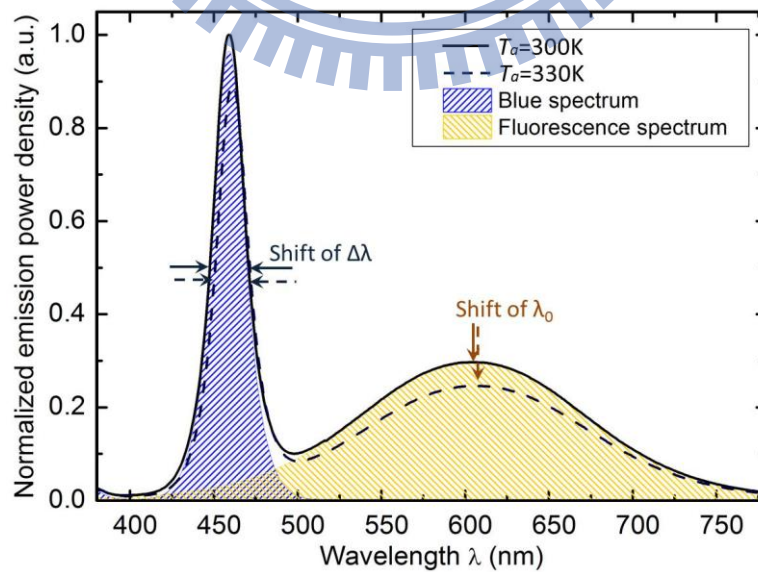


Figure 1-4 The spectrum of phosphor-converted white LED changes with respect to ambient temperature T_a .

However, which raises the question as to the predictability and stability of LED-based light sources. Such spectral distortion therefore results in the drift of chromaticity point, color rendering property, and efficiency of the LEDs cluster ^[11]. Taking a trichromatic mixing set of $\hat{\lambda}_1 = 455 \text{ nm}$ ($\Delta\lambda = 5.5 \text{ kT}$), $\hat{\lambda}_2 = 530 \text{ nm}$ ($\Delta\lambda = 7.9 \text{ kT}$), and $\hat{\lambda}_3 = 605 \text{ nm}$ ($\Delta\lambda = 2.5 \text{ kT}$) as an another example, which is designed for general lighting application. A slight shift of red peak wavelength from 605nm to 620nm will decrease the color rendering index *CRI* from 85 to 65 and the luminous efficacy of radiance *LER* from 320 *lm/watt* to 290 *lm/watt*, respectively. Similarly, a shift of green peak wavelength from 530 nm to 550 nm will decrease the *CRI* to the value less than 60, revealing that *CRI* is highly sensitive to the exact position of spectral peak ^[11].

The color rendering index *CRI* is a widely recognized figure of merit to evaluate the light quality of white light sources. Interested reader can refer to ref. [12] for more discussion about color appearance by various qualitative characteristics of lighting. The other figure of merit, the luminous efficacy of radiance *LER*, is defined as amount of luminous flux (lumen) converted per unit optical power (watt).

1.2.1 Prior arts in consideration of thermal and current issues

In order to solve aforementioned issues, many efforts have been made to model the dependence of LED spectra on the temperature and current. In terms of theoretical interpretation, the LEDs emission spectrum is described by the product of the density of energy states within the allowed energy band and a Boltzmann energy distribution ^[13]. Most recently A. Keppens et al introduced this underlying physic into H. Y. Chou's model, allowing for accurate simulations of single color LED spectra at any temperature ^{[14], [15]}. However, the difference between the experimental and the

quasi-physical model still needs to be empirically compensated.

In contrast to the physical consideration, mathematically using Gaussian function can simply incorporate the spectrum power distribution (*SPD*) with three spectral features ^[16]. In 2005, a more general model on the basis of double Gaussian function was developed by Y. Ohno, which is nowadays still used by CIE ^[17]. F. Reifegerste and J. Lienig, in 2008, evaluated the applicability of several mathematical functions for modeling of LED spectra; meanwhile, the formalism for low powered single-color LED in consideration of temperature and current was proposed ^[18]. Nevertheless, a large number of fitting parameters precludes its transfer to practical use. Although many spectral radiant flux models have been published so far, to our knowledge, there is still lack of an easy-to-use modeling approach for high powered single-color LED, which is capable of simply extending to the spectrum modeling of phosphor-converted white light.

1.3 Ideal multispectral mixing optimization

In general, the mixing of multiple spectra based on LEDs can be accomplished by using (i) additive mixing of two or more single-color LED chips (LED-primary-based approach), (ii) wavelength-conversion via using phosphors or other materials (LED-plus-phosphor-based approach), and (iii) a hybrid approach composed of (i) and (ii) ^[2]. In section 1.1, we have briefly discussed trichromatic mixing via LED-primary-based approach, where three emission sources for the trichromatic case are predetermined. Therefore, the linear system is critically determined. In fact, the selections of emission bands provide additional degrees of freedom, whose values will be highly relevant to the operational purposes. For example, a trichromatic combination of $\hat{\lambda}_1 = 450 - 455 \text{ nm}$ ($\Delta\lambda = 5 \text{ kT}$), $\hat{\lambda}_2 = 525 - 535 \text{ nm}$ ($\Delta\lambda = 5 \text{ kT}$),

and $\hat{\lambda}_3 = 600 - 615 \text{ nm}$ ($\Delta\lambda = 5 \text{ kT}$) is very favorable in terms of high color rendering lighting, resulting in a high *CRI* value in the range of 80–85 ^[11].

Now we generalize the condition by considering a synthesized SPD composed of n undetermined emission bands, used for certain purpose with specific chromaticity point. The problem is no longer critically determined but underdetermined, which is equivalent to subjecting the $2n$ -dimensional parameter space $\{ \hat{\lambda}_1, \dots, \hat{\lambda}_n, I_1, \dots, I_n \}$ to three color-mixing constrains. In other words, an optimization happens in searching the best location, composed by two n -dimensional vectors $\{ \hat{\lambda}_1, \dots, \hat{\lambda}_n \}$ and $\{ I_1, \dots, I_n \}$, on the hypersurface with dimensionality $2n - 3$. Where the best location represents that composed spectrum provides the maximal benefit to the purposes. We could mathematically write the solution in a form as:

$$\arg \max[\{MF, cons\} \{ \hat{\lambda}_1, \dots, \hat{\lambda}_n, I_1, \dots, I_n \}] \quad (1-8)$$

where MF is the merit function of the purposes. The term *cons* indicates three mixing constrains. In 2002, A. Žukauskasa et al. solved the above problem for general lighting applications ^[19]. For simplicity, each emission band was assumed as a single Gaussian line with $\Delta\lambda = 6 \text{ kT}$. The optimal LEDs clusters for $n = 2, 3, 4,$ and 5 were analyzed. Those results address the fundamental tradeoff between the luminous efficacy of radiance *LER* and the color rendering index *CRI*, which has the potential to provide a useful guide in the design of a polychromatic system.

1.4 Aspects regarding the practical realization of LEDs cluster

1.4.1 Spectral characteristic

To consider a practical system, first and foremost, more precise spectral characteristics should be imposed on sources instead of the artificial Gaussian distribution. In other words, the temperature and currents dependences of LEDs, as we mentioned in Section 1.2, should be predictable. In contrast to the ideal mixing condition, this additional temperature dependence results in the incensement of the dimensionality of the problem from $2n - 3$ to $3n - 3$. Equation (1-8) would be rewritten as:

$$\arg \max[\{MF, cons\} \{\hat{\lambda}_1, \dots, \hat{\lambda}_n, I_1, \dots, I_n, T_1, \dots, T_n\}] \quad (1-9)$$

Such high dimensionality however raises the difficulty on searching the solution to satisfy Equation (1-9). Therefore, crucial to this problem must be the dimensional reduction, e.g. using known types of sources. K. Man and I. Ashdown, in 2006, basically solved a mixing issue with three predetermined single-color LEDs. Their work presented an adaptive trichromatic LEDs cluster, which is capable of accurate colorimetric feedback over a range of temperature by modeling the sources with double Gaussian fit ^[20].

1.4.2 Color quality index

Another aspect that must be covered in the implementation of a practical spectral mixing is the development of more accurate figure of merits. In the field of general lighting, color rendering index *CRI* has been criticized for its lack of fidelity in ranking sources, especially for those having highly peaked spectra such as LEDs ^[21].

One of the major deficiencies is the penalization of sources that produce high-chromatic saturation, which is actually preferred for human vision ^[22]. As a consequence, numerous refinements have been explored, such as the color quality scale (*CQS*) ^[23], gamut area index (*GAI*) ^[24], and color saturation index (*CSI*) ^[25].

1.4.3 Energy evaluation

In addition, the figure of merit in terms of energy also has to be redefined as the luminous flux normalized to the electrical input power (watt) expended to operate the LED, which is equivalent to the product of the luminous efficiency of radiance *LER* and electric-to-optical power conversion efficiency ^[26]. It is obvious that this energy factor, namely luminous efficiency *LE*, will be equal to *LER* under the device with perfect electric-to-optical power conversion efficiency. *LE* is lately adopted by G. He *et al.* in 2010. In He's work, several di-, tri-, and tetrachromatic mixing cases using hybrid approach, under a constant temperature environment, were realized and analyzed over a range of color temperatures (*CTs*) ^[27], ^[28].

1.5 Motivation and objective of this thesis

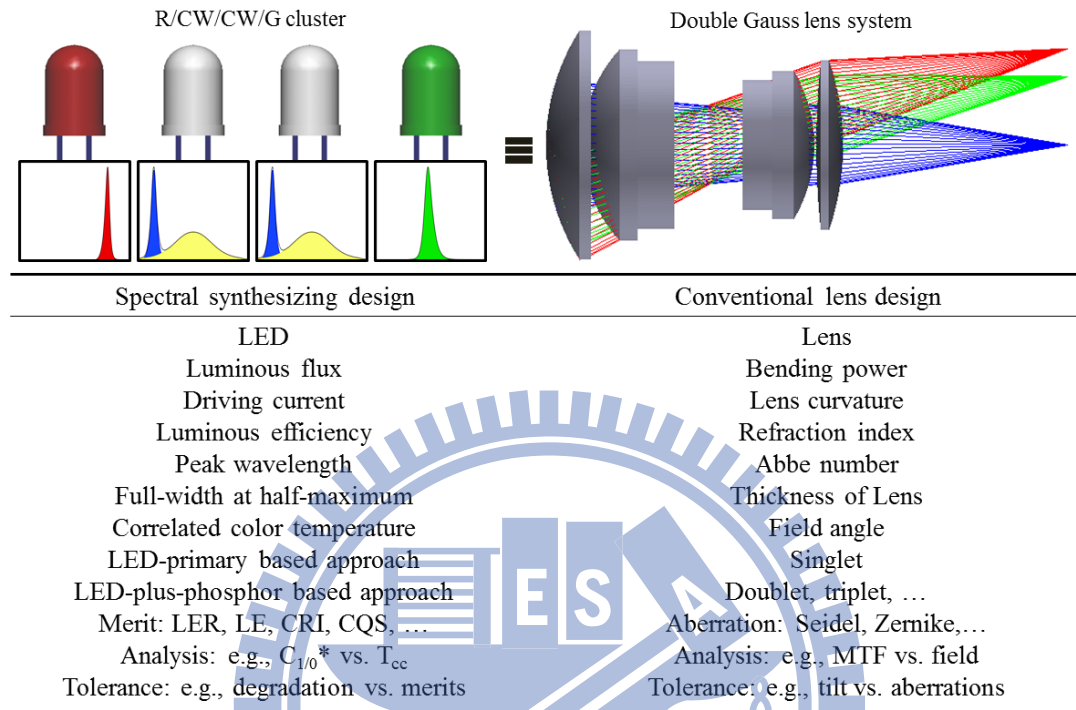
Up to this point, the ideal multispectral mixing and practical considerations have been discussed. As we mentioned in Section 1.4, the practical use of trichromatic mixing using LED-primary-based approach has been completed by K. Man and I. Ashdown ^[20]. Afterward, as the trend of higher efficiencies in phosphor-converted white LEDs continues, the possible hybrid designs increases as well ^[29]. State of the art tetrachromatic hybrid design (neutral-white/red/green/blue), proposed by G. He *et al.*, can realize a white composite light with high color rendering property as well as high luminous efficiency ^[27], but due to the assumption of constant thermal environment

(i.e. only consider the dependence of current on source model) a widespread diffusion of multichip LED cluster is not provided. To date, a general *SPD* synthesizing for practical LED clusters, especially for those with the number of sources > 3 , is still subject of discussion. Main obstacle lies in the present lack of complete methodology, which can systematically and efficiently optimize *SPD* for an underdetermined system in consideration of current and temperature dependences

In order to overcome current implementation barriers of LEDs cluster, we make an attempt to borrow design techniques from a conventional lens system to develop a general mixing approach in a more complete treatment. The idea arose from the recognition of the fundamental similarity of multi-chip LEDs system and conventional lens system. The whole design flow in all aspects can be closely analogous to a lens design process that has long been developed, by which the spectrum of an LED cluster can be optimized by going through every step of the proposed scheme.

In general, we emulate a single-color LED as a singlet, whose light-bending power determined by its curvature and refractive index can be conceptually analogous to the emitting luminous flux of an LED determined by the drive current and luminous efficiency LE , respectively. As we mix a number of LEDs, the additive mixing by two single-color LEDs is equivalent to two singlet lenses. Likewise, the LED-plus-phosphor-based approach can be regarded as a cemented doublet (dichromatic) or triplet (trichromatic), depending on the number of emitting peak wavelengths. The concept is schematized in Figure 1-5. Based on the outlined hypothesis, the *SPD* synthesis can be transformed into a classic lens design problem. For example, an LED cluster composed of red/cool-white/cool-white/green (R/CW/CW/G) is logically equivalent to a double Gauss lens system. The

fundamental constraint such as diffraction limitation of a lens system is regarded accordingly as the theoretical boundary of the LER.



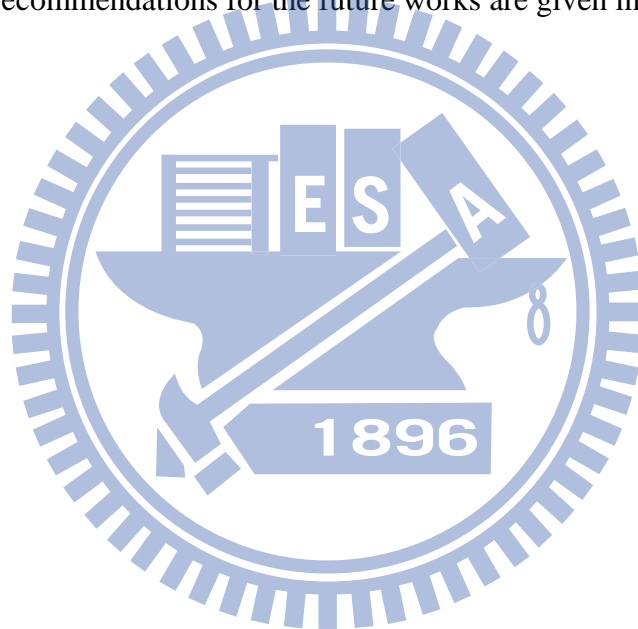
* The defined increment of CQS in section 2.4

Figure 1-5 Conceptual analogy between the *SPD* synthesis and conventional lens design. A LED cluster composed of red/cool-white/cool-white/green (R/CW/CW/G) can be regarded as a double Gauss lens system with two singlet lenses and two cemented doublets, where the cool-white LED is caused by dichromatic mixing.

1.6 Organization of this thesis

The thesis is organized as following: The complete treatment of LED spectrum characterization is provided in **Chapter 2**, including the junction temperature detection and determination, the LED spectrum modeling in terms of junction temperature and drive current, and the validation of the simulated spectrum model. In **Chapter 3**, the methodology of the multispectral mixing optimization is presented, which has six steps that in all aspects can correspond to the design flow of the

conventional lens system. By using the proposed methodology into practical LEDs system, we demonstrate two design cases for general lighting application in **Chapter 4**. The first example follows the design flow step-by-step to produce a color tunable LEDs cluster with high color rendering property as well as high efficiency. In the second design case, we further release the constraint of the constant ambient temperature, so that a more practical multispectral mixing platform can be realized. Furthermore, detailed analyses and comparison for different LEDs combination are also provided in this chapter. Finally, discussions and summary of this doctoral dissertation, and recommendations for the future works are given in **Chapter 5**.



Chapter 2

LED Spectral Characterization

2.0 Goal

In the traditional optical design, the dioptre, or diopter ϕ , is a unit of measurement of the optical power for a single lens, which can be expressed in terms of refractive index n and surface curvatures r_1, r_2 . In the first order optics, the expression for a thin lens can be written as:


$$\phi = \frac{1}{f} = (n-1)(r_1 - r_2) \quad (2-1)$$

where f is the focal length. The refractive index of optical glasses, in general, changes with ambient temperature, the extend of which depends on the glass type and on the wavelength^[30]. Therefore, the diopter of a lens can be characterized by temperature and surface curvatures. One benefit of using diopter (reciprocal of focal length) rather than focal length is that the linearity exists in power calculation of thin lens system. For example, a doublet system with a thin 2-dioptre lens close to a thin 0.5-dioptre lens would have the focal length approximated to that of a singlet with 2.5-dioptre.

For an additive mixing system, the corresponding assumption of narrower spectral bandwidth yields the linear property in chromaticity calculation as mentioned in Section 1.1. In addition, the factors conceptually analogous to the surface curvature and ambient temperature in lens system are the drive current I_{DC} and junction

temperature T_j . As we have known that I_{DC} and T_j are crucial bases for spectral model. The process that establishes the connection of spectrum power distribution SPD with drive current I_{DC} and junction temperature T_j can be named as the LED spectral characterization. In this chapter, we have an intention to provide a complete process and formalism in spectral characterization.

2.1 Junction temperature measurement

Due to the $p-n$ junction located deep inside the commercial LEDs package, real time junction temperature determination is almost impossible ^[31]. Many researches therefore reported several junction temperature measurement techniques, including the forward voltage method ^{[32], [33]}, the peak wavelength shift method ^[32], the high energy slope method ^[34], the nematic liquid crystal method ^{[35], [36]}, and the radiation energy method ^{[37], [38]}. Among these methods, the forward voltage method is utilized in this research because it is the most convenient way to incorporate the junction temperature detection into the control of drive current.

2.1.1 Forward voltage method

There are two main steps for the forward voltage method. The first one is to launch the pulsed calibration measurement to obtain the database of forward voltage V_f subject to a set of two parameters: junction temperature T_j and pulsed drive current I_p . By interpolating the data in the first step, it is likely to precise estimate the junction temperature from the corresponding forward voltage.

For the calibration measurement, five commercial available single-die high-power LEDs are selected, consisting of red, amber, green, blue, and cool-white emitters with the maximum input power of 1 watt. The sample LEDs are mounted

inside TeRchy HRMB-80 isothermal oven with active air circulation ^[39]. The oven temperature is predefined by every 10°C increment. To ensure the thermal steady state between the air in the oven and chip junction, at least thirty minutes delay between the settled temperature and the measurement is needed. Each sample LED then is driven by a pulsed current with low duty cycle (e.g. 0.1%), so that the additional thermal effect from the power dissipated in the chip junction can be neglected. Therefore, the junction temperature is logically equivalent to the oven temperature. During the pulse current applied, the voltage measurement is performed with the Keithley 2400 SourceMeter that controlled by our GUI program.

2.1.2 Junction temperature estimation

A typical forward current-voltage I_p-V_f characteristic at different junction temperature T_j is shown in Figure 2-1. According to different current level, the current-voltage character reveals three different tendencies. When the drive current $\leq 100\mu A$, the current exceeds the exponential fit (dashed line) because the measured character is dominated by various leakage currents. For example, one of these leakages is the carrier tunneling transport across the quantum-well structure ^[40]. For drive current $\geq 10mA$, the effect of the internal series resistance gradually dominate the character of the current-voltage curve, which results in a lower drive current ^[41]. In the ideal exponential fit region $100\mu A \leq I_p \leq 10mA$, the current-voltage characteristic of the p-n junction diode can be described by the Shockley equation ^[42]:

$$I_p = I_s \exp\left(\frac{eV_f}{n_{ideal}BT_j}\right) \quad (2-2)$$

The factors e and B indicate the elementary charge and the Boltzmann constant, respectively. I_s refers to the effective saturation current, the combination of two

saturation currents under diffusion and recombination process. n_{ideal} is the ideality factor with a theoretical value between 1 and 2.

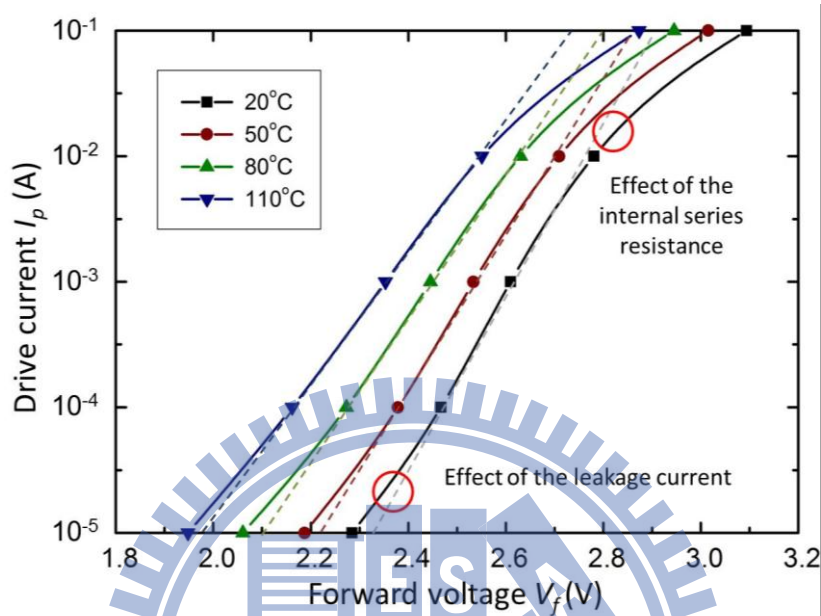


Figure 2-1 Typical semi-log current-voltage characteristic of a green InGaN LED (HELIO Optoelectronics Corp., HMHP-E1HG)

Subsequently, we attempt to establish the relation between forward voltage V_f and junction temperature T_j by examining five current levels, $10\mu\text{A}$, $100\mu\text{A}$, 1mA , 10mA , and 100mA from Figure 2-1. As shown in Figure 2-2, despite slight deviations from the linearity due to the effects of leakage current (see the high junction temperature side for current $I_p = 100\mu\text{A}$) and internal series resistance (see the low junction temperature side for current $I_p = 10\text{mA}$), a linear approximation has proven to be sufficient for junction temperature prediction for $100\mu\text{A} \leq I_p \leq 10\text{mA}$ ^[43], which is given as:

$$V_f(T_j) \approx \gamma(I_p)T_j + \delta \quad (2-3)$$

where γ and δ are the slope for a specific pulsed current I_p and the current independent intercept, respectively.

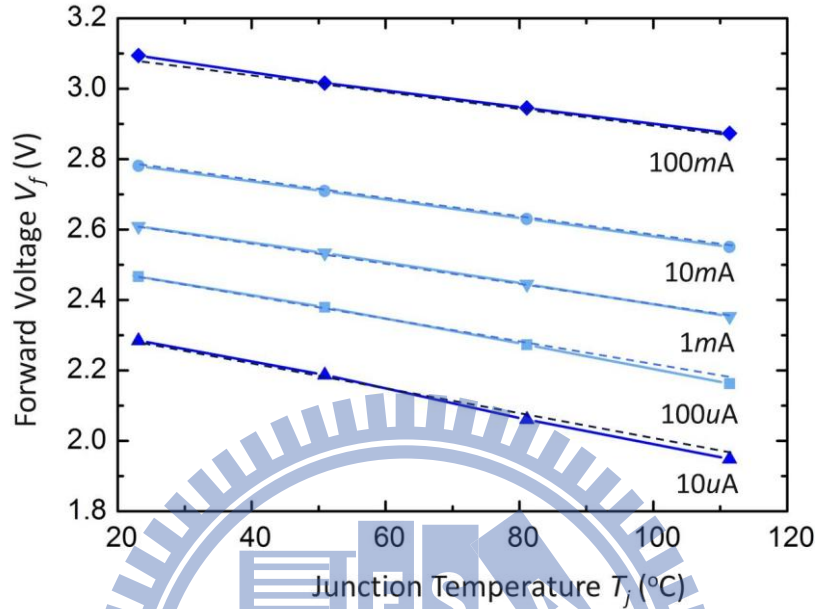


Figure 2-2 The voltage-temperature characteristic of a green InGaN LED (HELIO Optoelectronics Corp., HMHP-E1HG) at five current levels.

With the linear approximation, the slope γ and intercept δ of Equation (2-3) can be obtained from measuring only two voltage-temperature characteristics, $V_f(T_1)$ and $V_f(T_2)$, which prevents a time-consuming measurement. Where T_1 and T_2 can be the two extreme cases as the thermal boundary, i.e. $T_1 = 20$ °C and $T_2 = 110$ °C respectively. Therefore, a calibration curve that profiles the relationship between the forward voltage V_f and junction temperatures T_j can be rewritten as:

$$T_j \approx \frac{T_2 - T_1}{V_f(T_2) - V_f(T_1)} [V_f - V_f(T_1)] + T_1 \quad (2-4)$$

For the pulsed drive current $I_p > 100mA$, the behavior of the internal series resistance (R_s) should be taken into account. Thus the Equation (2-3) can be modified to an extended version^[43]:

$$V_f(T_j) \approx I_p R_s(T_j) + \gamma(I_0)T_j + \delta \quad (2-5)$$

In fact, junction temperature dependence of the internal series $R_s(T_j)$ for $I_p > 100mA$, like $V(T_j)$ in the region of $100\mu A \leq I_p \leq 10mA$, is often approximated by a linear expression as well, which could be simply written as $R_s(T_j) = \gamma' T_j + \delta'$ with slope and intercept γ' and δ' . The new slope $\gamma'' = \gamma' + \gamma$ and intercept $\delta'' = \delta' + \delta$ will be generated to fit the behavior in this region. Consequently, it is more convenient to stick with Equation (2-4) for practical junction temperature estimation, via only two measurements to obtain a set of parameters (γ, δ) or (γ'', δ'') . The results of the best fitting for all measured LEDs are gathered in Table 2-1. A good agreement between the experimental measurement and linear model can be obtained with R^2 exceeding 0.99.

Table 2-1 Pentachromatic LEDs, specific pulsed current I_p , slopes γ and γ'' , and intercepts δ and δ'' of the linear approximation.

LED (HELIO Optoelectronics Corp.)	$I_p = 1mA$		$I_p = 100mA$	
	γ	δ	γ''	δ''
HMHP-E1HR (red)	-1.91E-03	1.72	-1.82E-03	2.13
HMHP-E1HA (amber)	-2.19E-03	1.80	-1.74E-03	2.06
HMHP-E1HG (green)	-2.91E-03	2.68	-2.48E-03	3.18
HMHP-E1HB (blue)	-1.35E-03	2.43	-1.39E-03	2.82
HMHP-E1HW (cool-white)	-1.54E-03	2.56	-2.04E-03	2.98

2.2 Junction temperature determination

To this point, we have completed junction temperature estimation from the current-temperature calibration measurement. In the following step, sample device is operated under normal conditions, which is exposed to variant ambient temperature T_a and subjected to a series of DC drive current I_{DC} . With the help of previous calibration, the junction temperature determination can be achieved in terms of ambient temperature T_a and DC drive current I_{DC} directly.

We firstly apply a constant drive current I_{DC} through the sample LED mounted on a fixture (Arroyo Instruments, TEC 264-BB-DB9). The entire module is placed inside the cavity of an integrating sphere. The temperature of the fixture controlled by the thermoelectric cooler (Arroyo Instruments, TEC Source 5310) can be regarded as the ambient temperature T_a . As the thermal steady state has been reached, the DC forward voltage V_{DC} is recorded, and the emitted spectral power distribution SPD as well as the overall optical power Φ of each sample LED can be captured by the spectrometer (SR-UL1R, Topcon) attached to the integrating sphere. The junction temperature T_j can be determined by the interpolation of the DC forward voltage V_{DC} according to the pulsed calibration measurement. Finite sampling points are measured in a normal operation range ($10\text{ }^\circ\text{C} \leq T_a \leq 100\text{ }^\circ\text{C}$ and $0\text{ mA} \leq I_{DC} \leq 350\text{ mA}$), in which the incensements of ambient temperature and DC drive current are programed to be $10\text{ }^\circ\text{C}$ and 35 mA , respectively.

Based on the experimental setup, we could have measured results composed of one $M \times N$ spectral matrix \mathbf{S} and several $M \times 1$ parameter vectors, i.e. \mathbf{t}_j (junction temperature), \mathbf{t}_a (ambient temperature), ϕ (optical flux), \mathbf{v}_{DC} (DC forward voltage) and \mathbf{i}_{DC} (DC drive current). Where M represents the number of experimental modulations (here $M = 100$) and N is the number of sampling points uniformly distributed within

380nm to 780nm in steps of 10nm ($N = 41$). It is noted that vectors are denoted by bold-faced lower-case letters and matrices are represented by bold-faced capital letters.

With the sufficient database, the junction temperature T_j now can be related to ambient temperature T_a and DC drive current I_{DC} via the introduction of the equation developed by A. Keppens [44]:

$$T_j(I_{DC}, T_a) \approx \frac{R_t[c_1 I_{DC}^2 + c_2 I_{DC}] + T_a}{1 - R_t[c_3 I_{DC}^2 + c_4 I_{DC}]} \quad (2-6)$$

where c_1 , c_2 , c_3 , and c_4 are fitting parameters that can be easily calculated from importing variant known input data set (I_{DC} , T_a) and corresponded output data T_j , the fitting values for all sample devices at $T_a = 50^\circ\text{C}$ are shown in Table 2-2. In Equation (2-6), the thermal resistance R_t between the junction and the reference point can also be predetermined by inserting known values of T_j , T_a , $P_e (= I_{DC}V_{DC})$, and Φ to the following equation:

$$R_t = \frac{T_j - T_a}{P_e - \Phi} \quad (2-7)$$

In which the denominator, the difference of the input electric power P_e and the radiant flux Φ , indicates the power dissipated in the LED. The measurement results for red AlInGaP LED (HELIO Optoelectronics Corp., HMHP-E1HR) are shown in Table 2-3, where the resistance of $48.1^\circ\text{C}/\text{watt}$ can be determined.

Table 2-2 The values of fitting parameters c_1 , c_2 , c_3 , and c_4 for pentachromatic LEDs at ambient temperature $T_a = 50$ °C.

LED (HELIO Optoelectronics Corp.)	Fitting parameters			
	c_1	c_2	c_3	c_4
HMHP-E1HR (red)	- 0.0420	0.0685	- 2.8118	- 1.4573
HMHP-E1HA (amber)	- 0.0996	0.1972	- 2.8791	- 7.3223
HMHP-E1HG (green)	- 0.5543	0.7596	21.2939	- 35.8853
HMHP-E1HB (blue)	- 0.0039	- 0.0107	3.8395	1.7290
HMHP-E1HW (cool-white)	- 0.0669	0.0927	- 1.5967	- 3.0327

Table 2-3 The DC drive current I_{DC} , electrical power P_e , optical power Φ and junction temperature T_j for red AlInGaP LED (HELIO Optoelectronics Corp., HMHP-E1HR) at ambient temperature $T_a = 50$ °C.

I_{DC} (mA)	P_e (watt)	Φ (watt)	T_j (°C)
70	0.143	0.202	56.9
140	0.307	0.429	64.8
210	0.495	0.676	73.8
280	0.697	0.935	83.5
350	0.915	1.208	94.0

2.3 LED spectrum modeling

2.3.1 Double Gaussian model

Generally, the spectral power distribution SPD can be fitted by a single Gaussian function, which incorporates three the power (p), peak wavelength ($\hat{\lambda}$) and spectral width ($\Delta\lambda$) with junction temperature. However, in most of cases, practical spectrum is not perfectly symmetric, which will lead to the numerical error by single Gaussian fitting. In order to overcome this issue, in this chapter, we proposed a double Gaussian function with two sets of parameters: $(p, \hat{\lambda}, \Delta\lambda)$ and $(p', \hat{\lambda}', \Delta\lambda')$. On the basis of the discussion in Section 1-2, all parameters related to the spectrum are supposed to be functions of both junction temperature T_j and DC drive current I_{DC} . The estimated spectrum composed by the double Gaussian function, in contrast with the measured spectrum S , is denoted as \tilde{S} . Therefore, an estimated $M \times N$ spectral matrix $\tilde{\mathbf{S}}$ (e.g. $M = 100$ and $N = 41$ respectively) for a single-color LED can be expressed as:

$$\tilde{\mathbf{S}} = \mathbf{G} + \mathbf{G}' \quad (2-8)$$

where $\mathbf{G} = (\mathbf{g}_1, \dots, \mathbf{g}_M)^T$ and $\mathbf{G}' = (\mathbf{g}'_1, \dots, \mathbf{g}'_M)^T$ represent two Gaussian bases of the double Gaussian spectral matrix. Here we can temporarily omit \mathbf{G}' and solely focus on \mathbf{G} due to the same treatment for both of them from Equation (2-8) to Equation (2-10). The base matrix \mathbf{G} has M spectral vectors \mathbf{g}_1 to \mathbf{g}_M , each of them has N sampling wavelengths. The value for the n th point of m th row vector \mathbf{g}_m , named as g_{mn} , can be given by:

$$g_{mn} = p_m \exp\{-[\lambda_n - (\hat{\lambda})_m]^2 / \Delta\lambda_m^2\} \quad (2-9)$$

where three parameters p_m , $\hat{\lambda}_m$, and $\Delta\lambda_m$ refer to the m th Gaussian power, peak wavelength, and spectral width of the base matrix \mathbf{G} , whose values could be found by satisfying the minimization of Equation (2-10) :

$$\arg \min[\|\mathbf{s}_m - \tilde{\mathbf{s}}_m\|^2, \{p_m, \hat{\lambda}_m, \Delta\lambda_m, p'_m, \hat{\lambda}'_m, \Delta\lambda'_m\}] \quad (2-10)$$

where \mathbf{s}_m is the m th measured spectrum (m th vector) of the spectral matrix \mathbf{S} , and $\tilde{\mathbf{s}}_m = \mathbf{g}_m + \mathbf{g}'_m$ is the estimated spectrum, corresponding to \mathbf{s}_m , of the spectral matrix $\tilde{\mathbf{S}}$.

2.3.2 Single-colour spectral function

After applying the minimization of Equation (2-10) through the spectral matrix, we have three $M \times 1$ vectors including Gaussian power \mathbf{p} , peak wavelength $\hat{\lambda}$, and spectral width $\Delta\lambda$ that can empirically be related to junction temperature \mathbf{t}_j and DC drive current \mathbf{i}_{DC} :

$$\ln(\mathbf{p}) = \mathbf{M}_p \mathbf{c}_p \quad (2-11a)$$

$$\hat{\lambda} = \mathbf{M}_\lambda \mathbf{c}_\lambda \quad (2-11b)$$

$$\ln(\Delta\lambda) = \mathbf{M}_{\Delta\lambda} \mathbf{c}_{\Delta\lambda} \quad (2-11c)$$

where $\mathbf{M}_p = [\mathbf{t}_j^T \ln(\mathbf{t}_j) \ln(\mathbf{i}_{DC}) \mathbf{1}]$, $\mathbf{M}_\lambda = [\mathbf{t}_j \ln(\mathbf{i}_{DC}) \mathbf{1}]$ and $\mathbf{M}_{\Delta\lambda} = [\mathbf{t}_j \ln(\mathbf{t}_j)^{-1} (\mathbf{i}_{DC})^{1/2} \mathbf{1}]$ are

$M \times 3$ basis matrices for \mathbf{p} , $\hat{\lambda}$ and $\Delta\lambda$, respectively. The vector element $\mathbf{1}$ indicates

the $M \times 1$ all-ones vector. \mathbf{c}_p , \mathbf{c}_λ , and $\mathbf{c}_{\Delta\lambda}$ refer to 3×1 coefficient vectors, whose values could be calculated by linear least square method, e.g. power coefficient vector $\mathbf{c}_p = (\mathbf{M}_p^T \mathbf{M}_p)^{-1} \mathbf{M}_p^T \ln(\mathbf{p})$. For the red AlInGaP LED (HMHP-E1HR), Figure 2-3 shows the distribution of all elements in Gaussian power \mathbf{p} and its coefficient values c_{p1} , c_{p2} and c_{p3} . The corresponded goodness of fit, shown in Figure 2-4, reveals that the Gaussian power distribution is well fitted by Equation (2-11a).

Similarly, applying the above regularized process Equation (2-9) – Equation (2-11) to the other Gaussian function \mathbf{G}' will lead to coefficient vectors \mathbf{c}_p' , \mathbf{c}_λ' , and $\mathbf{c}_{\Delta\lambda}'$. By obtaining all of the coefficients, the complete double Gaussian function $\tilde{S}(\lambda)$ for single-color LED spectrum can be given in respect of the junction temperature T_j and DC drive current I_{DC} :

$$\begin{aligned} \tilde{S}(\lambda) &= G + G' \\ &= \exp[\mathbf{m}_p \mathbf{c}_p - (\lambda - \mathbf{m}_\lambda \mathbf{c}_\lambda)^2 / \exp(\mathbf{m}_{\Delta\lambda} \mathbf{c}_{\Delta\lambda})^2] \\ &\quad + \exp[\mathbf{m}_p' \mathbf{c}_p' - (\lambda - \mathbf{m}_\lambda' \mathbf{c}_\lambda')^2 / \exp(\mathbf{m}_{\Delta\lambda}' \mathbf{c}_{\Delta\lambda}')^2] \end{aligned} \quad (2-12)$$

where $\mathbf{m}_p = [T_j \ln(T_j) \quad \ln(I_{DC}) \quad 1]$, $\mathbf{m}_\lambda = [T_j \quad \ln(I_{DC}) \quad 1]$, and $\mathbf{m}_{\Delta\lambda} = [T_j \ln(T_j)^{-1} \quad (I_{DC})^{1/2} \quad 1]$

account for basis vectors of the Gaussian power (P), peak wavelength ($\hat{\lambda}$) and spectral width ($\Delta\lambda$) with variables T_j and I_{DC} .

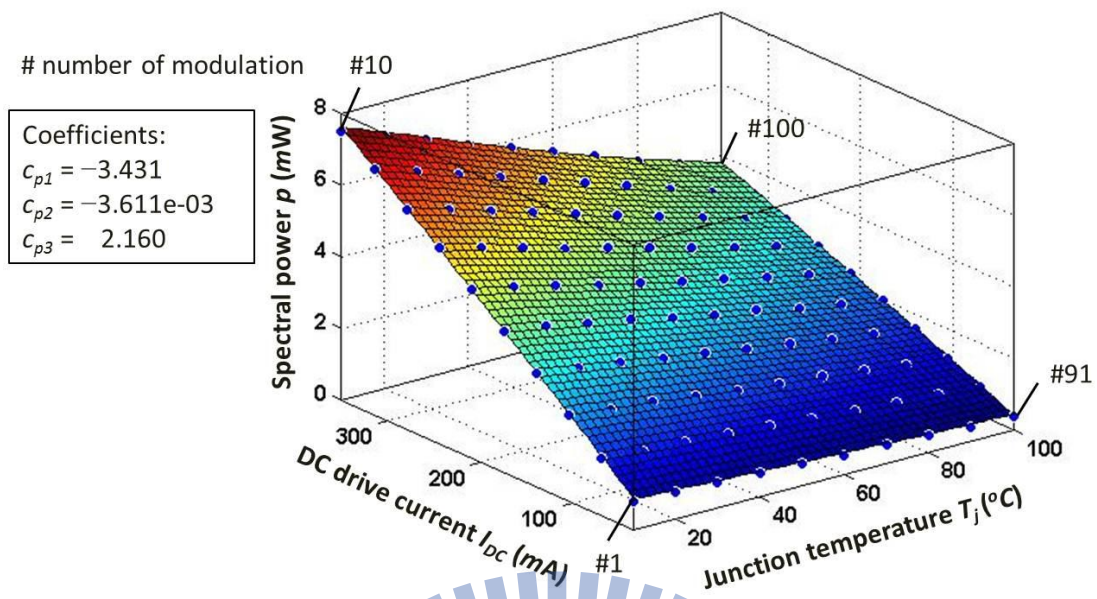


Figure 2-3 The distribution of all elements in Gaussian power \mathbf{p} and its fitting coefficient values c_{p1} , c_{p2} and c_{p3} .

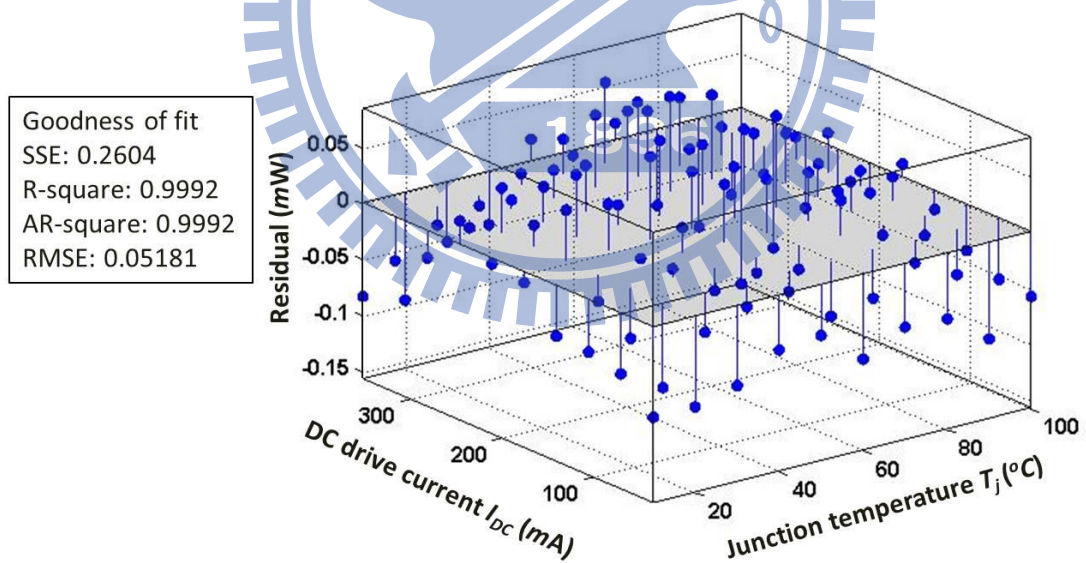


Figure 2-4 The deviation and goodness of fit for Gaussian power distribution fitting.

2.3.3 Phosphor-converted spectral function

For the spectrum of phosphor-converted white LED $S_w(\lambda)$, the estimated spectrum $\tilde{S}_w(\lambda)$ is simply assumed to be composed of two double Gaussian functions $\tilde{S}_B(\lambda)$ and $\tilde{S}_F(\lambda)$:

$$\tilde{S}_w(\lambda) = \tilde{S}_B(\lambda) + \tilde{S}_F(\lambda) \quad (2-13)$$

where $\tilde{S}_B(\lambda) = G_B + G_B'$ and $\tilde{S}_F(\lambda) = G_F + G_F'$ denote the double Gaussian in the blue region and the fluorescence region, respectively. Here a cutoff wavelength λ_{BF} should be defined to denote the boundary in the middle of blue and fluorescence component, whose value can be pointed when the slope of measured spectrum just changes from negative to positive. Therefore, the modeling of the spectrum $\tilde{S}_B(\lambda)$ follows the same mathematical treatment in single-color case from Equation (2-9) to Equation (2-12). The other spectrum $\tilde{S}_F(\lambda)$, however, can subsequently be found by the same way but using the modified target spectrum $|S_w(\lambda) - \tilde{S}_B(\lambda)|$.

2.4 Validation of the spectral model

In order to validate the spectrum models presented in Equation (2-12) and Equation (2-13). The simulation results as well as the measurement data for green and phosphor-converted LED emission spectra at $T_j = 25\text{ }^\circ\text{C}$ and $I_{DC} = 350\text{ mA}$ are correspondingly illustrated in Figure 2-5. The results show that a good agreement between the experiment and numerical approximation could be obtained with R^2 exceeding 0.98. The fitting parameters of estimated phosphor white light spectrum, determined from Equation (2-11), are to be listed in Table 2-4. Furthermore, the luminous flux and CIE colour coordinates for all sample LEDs are calculated and compared in Table 2-5.

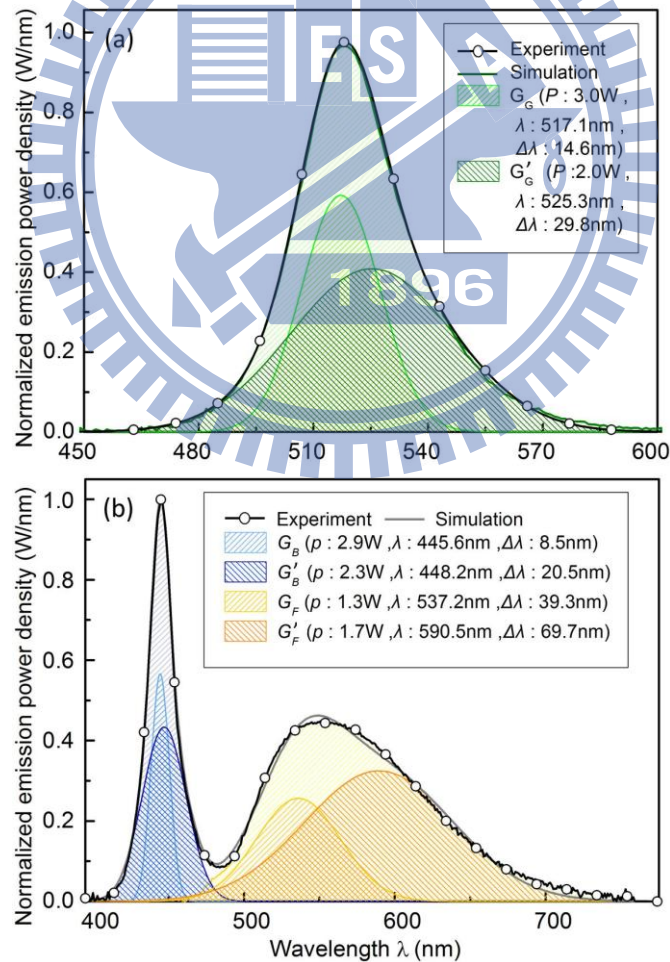


Figure 2-5 The illustration of the simulation model and the experimental measurement for green and phosphor LED spectra at $T_j = 25\text{ }^\circ\text{C}$ and $I_{DC} = 350\text{ mA}$, respectively.

Table 2-4 The parameters of approximated phosphor-converted LED spectrum. The blue and fluorescence components should be individually considered.

$$\tilde{S}_W(\lambda) = \tilde{S}_B(\lambda) + \tilde{S}_F(\lambda)$$

	G_B	G_F		G_B'	G_F'
c_{p1}	-4.1322	-4.8712	c_{p1}'	-4.5411	-4.5641
c_{p2}	-0.0051	0.0003	c_{p2}'	-0.0010	-0.0009
c_{p3}	2.0739	2.2380	c_{p3}'	2.1244	2.1370
$c_{\lambda 1}$	450.0824	539.5471	$c_{\lambda 1}'$	453.8196	561.7751
$c_{\lambda 2}$	0.0552	0.0340	$c_{\lambda 2}'$	0.0330	-0.0375
$c_{\lambda 3}$	-2.0052	0.4289	$c_{\lambda 3}'$	-2.5025	-4.3316
$c_{\Delta \lambda 1}$	2.0876	2.9537	$c_{\Delta \lambda 1}'$	3.6268	4.4596
$c_{\Delta \lambda 2}$	-0.0030	0.0038	$c_{\Delta \lambda 2}'$	0.0079	0.0022
$c_{\Delta \lambda 3}$	0.0047	0.0020	$c_{\Delta \lambda 3}'$	0.0023	0.0053

Table 2-5 The comparison of the simulation and measurement on luminous flux and CIE colour coordinates for all sample LEDs.

LED (HELIO Optoelectronics Corp.)	Measurement		Simulation		Deviation	
	$\Phi_v(lm)$	(x, y)	$\Phi_v(lm)$	(x, y)	$\Delta\Phi_v(\%)$	Δxy
HMHP-E1HR (red)	49.2	(0.6968, 0.3021)	49.0	(0.6994, 0.3004)	0.41	3.1e-3
HMHP-E1HA (amber)	46.5	(0.5841, 0.4155)	46.3	(0.5868, 0.4125)	0.43	4.0e-3
HMHP-E1HG (green)	81.4	(0.1592, 0.7086)	77.8	(0.1558, 0.7175)	0.44	9.2e-3
HMHP-E1HB (blue)	30.1	(0.1259, 0.0679)	29.7	(0.1295, 0.0639)	1.33	4.8e-3
HMHP-E1HW (cool-white)	115.1	(0.3195, 0.3408)	117.9	(0.3172, 0.3361)	2.43	5.3e-3

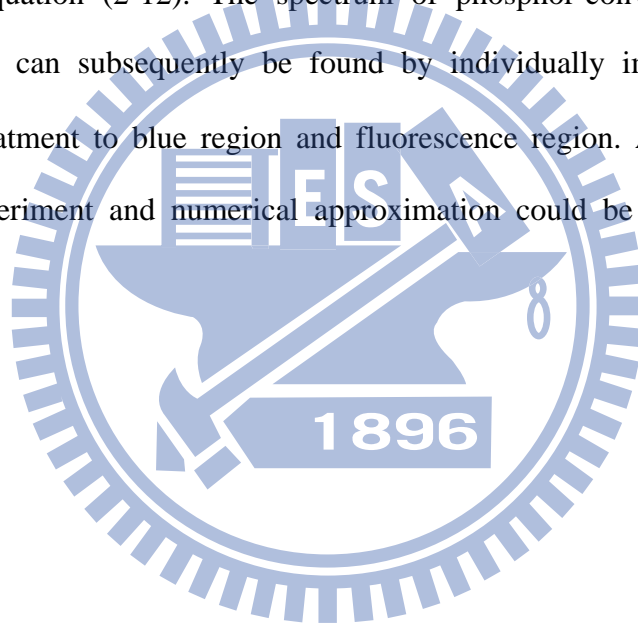
2.5 Summary and conclusions

Current-voltage characteristics for five sample LEDs have been measured at four junction temperatures from 20°C to 110°C. By examining different current levels, a linear approximation of Equation (2-4) can be used to describe the relation between the forward voltage V_f and junction temperatures T_j . Afterward, the current-voltage characteristics have been recorded at different ambient temperatures T_a as well. The result allowed deriving the thermal resistance R_t between the junction and the reference point. Thus the junction temperature T_j can directly be related to ambient

temperature T_a and DC drive current I_{DC} by Equation (2-6).

In the section of spectrum modeling, a double Gaussian function has been proposed to numerically fit practical spectra that are usually not perfectly symmetric.

The features of the Gaussian function, the power (p), peak wavelength ($\hat{\lambda}$) and spectral width ($\Delta\lambda$), can empirically be related to junction temperature T_j and DC drive current I_{DC} as given by Equation (2-11). Once all of the related coefficients are obtained, the double Gaussian function $\tilde{S}(\lambda)$ for single-color LED spectrum will be completed as Equation (2-12). The spectrum of phosphor-converted white LED $S_w(\lambda)$, however, can subsequently be found by individually imposing the same mathematical treatment to blue region and fluorescence region. A good agreement between the experiment and numerical approximation could be achieved with R^2 exceeding 0.99.



Chapter 3

Multispectral Mixing Optimization as Lens Design Techniques

3.0 Goal

The solution of lens design is a typical inverse problem. Given the effective focal length (EFL) and degree of correction for an optical system, it is always possible to determine the curvatures, the thicknesses, and the number of lenses accordingly. For example, if we aim to design a lens system with a specified EFL and correct three Seidel aberration coefficients, it can be analytically resolved by a set with two singlet lenses, that leaves four degrees of freedom, two powers and two shape factors [the shape factor is defined as $(R_2 + R_1) / (R_2 - R_1)$, where R_1 and R_2 are the radii of the first and second surfaces, respectively] ^[45]. However, due to the complexity of multiple lenses that increases the computational cost, the more efficient method in lens design would resort to an iterative process ^[46], as shown in Figure 3-1(a).

In multispectral mixing, a similar problem inspired us to borrow this process by replacing the lens set with a number of LEDs for a certain predefined requirements. The corresponded design procedure is proposed in Figure 3-1(b), including six steps: (3.1) initial system, (3.2) define boundary condition, (3.3) optimization, (3.4) aberration or merit analysis, (3.5) judgment, and (3.6) tolerance analysis. The aim of this chapter is to step by step complete the optimization process.

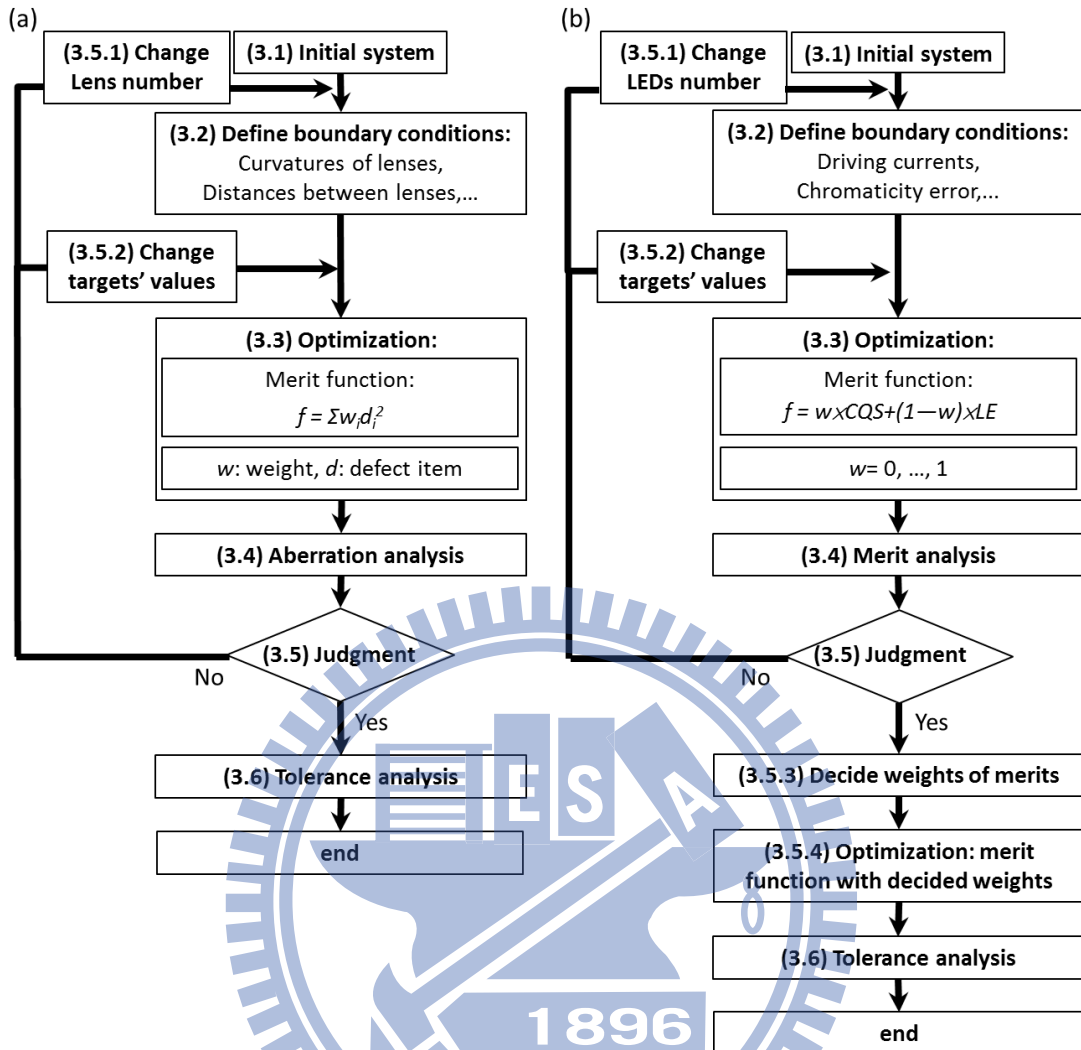


Figure 3-1 Design procedure of (a) lens design and (b) spectral synthesis of a LED cluster. Both flow charts include six steps: (3.1) initial system, (3.2) define boundary condition, (3.3) optimization, (3.4) aberration or merit analysis, (3.5) judgment, and (3.6) tolerance analysis.

3.1 Initial system

Like the glass map with variant lenses in lens design, a “LED map” with broad range of LEDs could be accordingly generated based on the manufacturers’ datasheets that offer different available materials and peak wavelengths ^{[47], [48]}. Because it is known that the LEDs with higher luminous efficiency possess higher emission flux, the luminous efficiency of a LED can be conceptually analogous to the refractive index, the y-axis of the glass map, of a lens. On the other hand, we replace the Abbe number, the x-axis of the glass map, by the peak wavelength for no good reason. Thus a LED map can be subsequently plotted as Figure 3-2. It is obvious that green (505nm) and amber (595nm)-colour LEDs would serve as the appropriate candidates in the consideration of high luminous efficiency,.

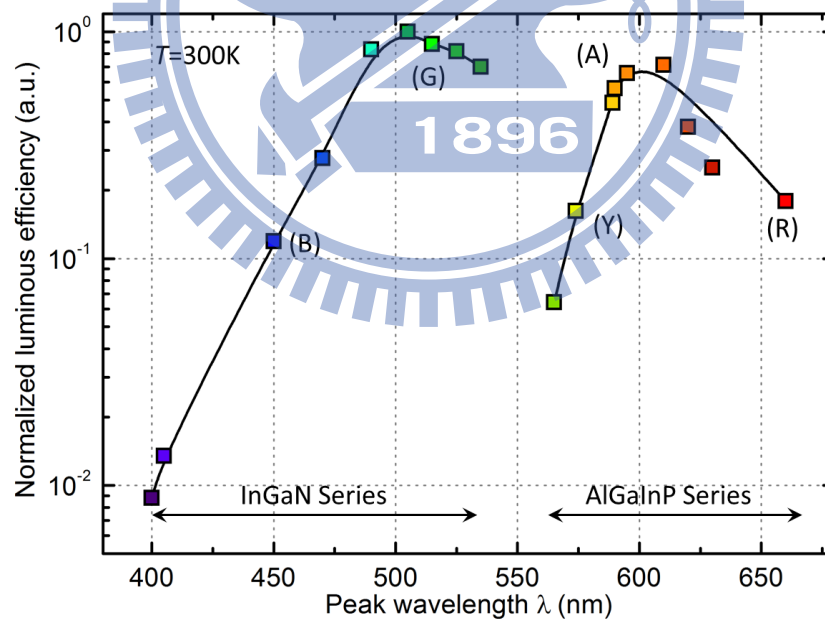


Figure 3-2 Normalized luminous efficiency of visible LED made from GaInN and AlGaInP series versus individual peak wavelength. The LED with high LE is analogous to the lens with high refractive index.

If we plan to mix two single-colour LEDs for a specific color temperature CT , the most straightforward solution is to select two complementary peak wavelengths on the chromaticity diagram. However, the question becomes more complex while multiple figures of merit are considered by a number of LEDs. To pick appropriate LED set in a systematic way, we list three suggestions for initial system ^[46]:

1. A mental guess. This way is workable for an expert while it is laborious for a beginner.
2. A designed case in previous literatures. It is the most common way to choose a design close to your requirements.
3. A search through the patent files. This is also a time-consuming work and the consideration of avoiding the patent's claims in your design is necessary.

At this moment, the second approach is easier to follow and, fortunately, many previous literatures have disclosed their experience for specific merits, e.g., the trichromatic source composed of primary emissions (630 nm, 530nm, and 450nm) makes surface colors appear more saturated, whereas the continuous spectrum designed to mimic daylight will have better color rendering ability ^[49]. In addition to single-colour LEDs, the rapid progress in efficiency of phosphor based LEDs will certainly drive the solid state lighting into more composite possibility ^[50].

3.2 Define boundary conditions

Before optimizing a predetermined initial system, the designer must define the domains of input variables. Such step not only ensures a reasonable result but also reduces the computational time. In lens design we usually set the curvatures and the thicknesses of lenses as the free variables to be optimized, whose domains are mainly constrained by the manufacturing feasibility. In terms of LEDs, previous work in Chapter 2 has pointed out that the variations of spectrum power distribution SPD and related characters (power p , peak wavelength $\hat{\lambda}$ and spectral width $\Delta\lambda$) for each LED component could be characterized by the driving current I_{DC} and the junction temperature T_j . In Chapter 2 we also have shown that the free variable T_j can further be related to ambient temperature T_a and drive current I_{DC} via Equation (2-6). Therefore, the drive current I_{DC} and ambient temperature T_a are chosen to be independent variables for boundary condition setting.

In general, the drive current I_{DC} for each LED has its physical limitation, either the operation range suggested by the manufacturer or the specific current with the radiant flux that has reached the target value. The mathematical description can be given as:

$$0 < I_{DC} < \max I_{DC} \quad (3-1a)$$

$$\max I_{DC} = \min[(\max I_{DC} \text{ in datasheet}), (\max I_{DC} \text{ when } \Phi = \Phi_T)] \quad (3-1b)$$

For the other free variable, T_a , the operation range of LED is determined by the temperature-controllable equipment, e.g. the oven in the calibration measurement or the thermoelectric cooler in the T_j prediction step (see Section 2.1 in Chapter 2).

In systematical point of view, however, an additional confinement to the chromatic deviation should be imposed for general lighting application. The deviation of $\Delta xy < 0.01$ is commonly used in lighting industry ^[51].

$$\|(x, y) - (x_T, y_T)\| < 0.01 \quad (3-2)$$

where (x_T, y_T) indicates the target chromaticity point.

3.3 Optimization

3.3.1 Metamerism

For the lens design, it is likely to have identical effective focal length EFL by variant combinations of curvatures and thicknesses from a prescribed lens system. Therefore, an additional mechanism of assessment, by adopting a merit function, is necessary for the selection of the optimized combination. The merit function of a lens system generally includes several aberrations and has the function of evaluating the impact of each parameter's change on image quality.

Similar condition can be found in the multispectral mixing system. Different SPDs subject to different combinations of driving currents might have equal color temperature (CT) (and even luminous level), called the metamerism ^[52]. Such metameric will provide different CIE tristimulus values for a reflecting test sample if illuminated with one spectrum or the other, leading to the light quality variation of the source. It goes without saying that a merit function composed of the plural of merit figure is needed, and then a decent optimization would be helpful in extracting the optimal combination of drive currents for clinic use. Detailed process will be presented as follows.

We firstly consider a multispectral mixing with K -type LED emitters, $K > 3$, which is underdetermined in language of linear algebra. A required tristimulus vector $\mathbf{t} = [X \ Y \ Z]^T$ is predetermined as the fixed target that the system must reach, whereas current tristimulus vector $\tilde{\mathbf{t}}$ is far from it. Where $\tilde{\mathbf{t}}$ is given by:

$$\tilde{\mathbf{t}} = \mathbf{C}_M \tilde{\mathbf{s}} \quad (3-3)$$

The $3 \times N$ matrix \mathbf{C}_M is the sampled color matching functions with dimension N . The spectrum $\tilde{\mathbf{s}}$ is synthesized from K -type LED spectra modeled by Equation (2-12) or Equation (2-13) in Chapter 2. Because each type of LED has two implicit free variables junction temperature T_j and drive current I_{DC} , the synthesized spectrum $\tilde{\mathbf{s}}$ basically represents an $N \times 1$ vector with $2K$ variables:

$$\tilde{\mathbf{s}} = \tilde{\mathbf{s}}[(T_j)_1, \dots, (T_j)_K, (I_{DC})_1, \dots, (I_{DC})_K] \quad (3-4)$$

It is obvious that, by brining Equation (3-4) into Equation (3-3), degrees of freedom for the multispectral system would be $2K - 3$. However, the solution for this system is not straightforward due to high degrees of freedom and implicit variables. In order to solve this issue, we suppose the ambient temperature T_a is uniformly distributed over a localized area with a small group of LEDs. Therefore the junction temperature T_j for each type LED can be determined from Equation (2-6) once T_a and I_{DC} are given. This assumption, however, degenerates the degrees of freedom $2K - 3$ into $K - 3 + 1$. Furthermore, we attempt to convert the implicit variables to be explicit by directly relating the tristimulus values to drive currents, where a $(2K + 1) \times 1$ quadratic current basis $\mathbf{i}_{qu} = [I_{DC} \ (I_{DC})_1 \ (I_{DC})_1^2 \ (I_{DC})_2 \ (I_{DC})_2^2 \ \dots \ (I_{DC})_k \ (I_{DC})_k^2]^T$ have empirically

been found to be sufficient to precisely characterize current tristimulus vector $\tilde{\mathbf{t}}$ under a specific ambient temperature T_a . In sum, the Equation (3-3) can be transferred to a version with lower degrees of freedom:

$$\tilde{\mathbf{t}} = \mathbf{C}\mathbf{i}_{qu} \quad (3-5)$$

where \mathbf{C} is a $3 \times (2K + 1)$ coefficient matrix. Noted that the degrees of freedom for Equation (3-5) turn out to be $K - 3 + 1 - 1$ owing to the imposed condition of the constant T_a . Thus, the metamerism (system is underdetermined) happens when the condition is identical to that we set in the first place, that is $K > 3$.

Now we could set current tristimulus values as our target $\mathbf{t} = \tilde{\mathbf{t}}$. However, the number of solutions for a metameric system is infinite, corresponding to infinite spectral distributions. It is needed to downsize the solution range to a finite randomized set, named as the initial current population \mathbf{I}_{DCP} that can be given as:

$$\mathbf{I}_{DCP} = [\mathbf{i}_1 \ \mathbf{i}_2 \ \dots \ \mathbf{i}_{m-1} \ \mathbf{i}_m]^T \quad (3-6)$$

Each row of the initial population is composed of K drive currents, which could be generated by two subsequent steps:

1. Randomly choose values for $K-3$ drive currents so that the system $\mathbf{t} = \tilde{\mathbf{t}}$ is transferred to be critical (three stimulus equations with three current unknowns).
2. Solve the critical system to obtain three positive solutions for the remained currents.

With the initial current population, \mathbf{I}_{DCP} , the corresponded initial junction temperature population, \mathbf{T}_{jp} , is readily obtained by sequentially introducing each element of \mathbf{I}_{DCP} and the constant temperature T_a into Equation (2-6). Similarly, the initial synthesized spectral population, $\tilde{\mathbf{S}}_{\text{p}}$, comes out by bringing the corresponded T_j and I_{DC} from \mathbf{T}_{jp} and \mathbf{I}_{DCP} into Equation (2-12) or Equation (2-13) for single-color or phosphor-converted LEDs, respectively, which can be expressed as:

$$\tilde{\mathbf{S}}_{\text{p}} = [\tilde{s}_1 \ \tilde{s}_2 \ \dots \ \tilde{s}_{m-1} \ \tilde{s}_m]^T \quad (3-7)$$

Obviously there is one-to-one correspondence between rows in $\tilde{\mathbf{S}}_{\text{p}}$ and \mathbf{I}_{DCP} .

3.3.2 Continuous genetic algorithm

From now on, we start to adopt a globe searching engine, continuous genetic algorithm (CGA) [53], to obtain the optimal composite spectrum as well as drive currents in terms of merit figures. The schematic process is shown in Figure 3-3. Detailed mathematical treatment applied to each step is described as follows:

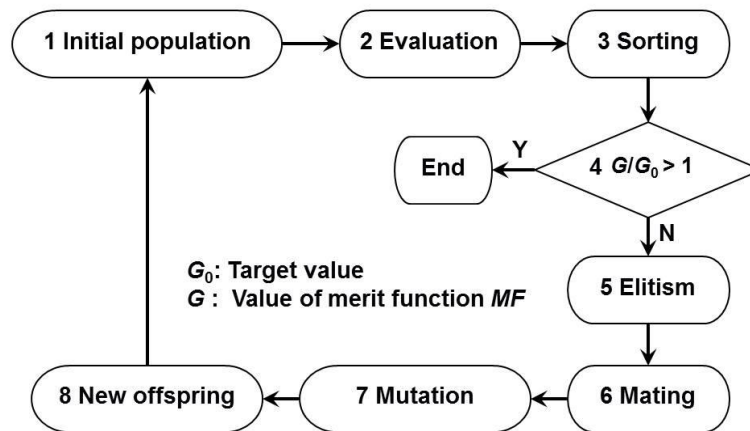
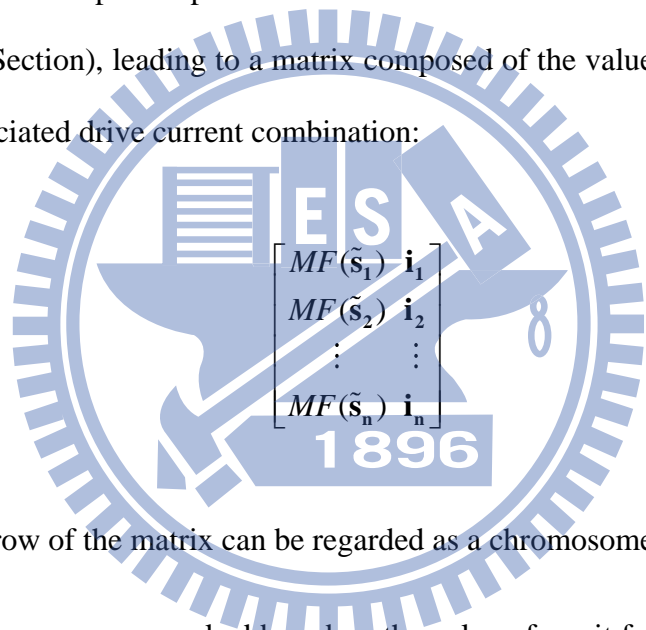


Figure 3-3 Schematic process of the continuous genetic algorithm (CGA).

1. First of all, an initial population matrix composed of spectral part and current part is randomly generated. Here the elements are gathered from the Equation (3-6) and Equation (3-7):

$$\begin{bmatrix} \tilde{\mathbf{s}}_1 & \mathbf{i}_1 \\ \tilde{\mathbf{s}}_2 & \mathbf{i}_2 \\ \vdots & \vdots \\ \tilde{\mathbf{s}}_n & \mathbf{i}_n \end{bmatrix} \quad (3-8)$$

2. We evaluate the spectral part via a user defined merit function MF (refer to the subsequent Section), leading to a matrix composed of the value of merit function and the associated drive current combination:



$$\begin{bmatrix} MF(\tilde{\mathbf{s}}_1) & \mathbf{i}_1 \\ MF(\tilde{\mathbf{s}}_2) & \mathbf{i}_2 \\ \vdots & \vdots \\ MF(\tilde{\mathbf{s}}_n) & \mathbf{i}_n \end{bmatrix} \quad (3-9)$$

where each row of the matrix can be regarded as a chromosome.

3. The chromosomes are ranked based on the value of merit function, which will result in a sorted matrix, as shown in Equation (3-10), with the optimal chromosome in the first row.

$$\begin{bmatrix} MF(\tilde{\mathbf{s}}_1') & \mathbf{i}_1' \\ MF(\tilde{\mathbf{s}}_2') & \mathbf{i}_2' \\ \vdots & \vdots \\ MF(\tilde{\mathbf{s}}_n') & \mathbf{i}_n' \end{bmatrix} \quad (3-10)$$

4. Compare the best value of merit function, $G = MF(\tilde{\mathbf{s}}_1')$, to the target value G_0 . If the ratio is smaller than unity, the spectrum should be further modified.

5. Under a process of natural selection, the survivors are chosen as the first half ranked chromosomes deemed fit enough to mate and to afford new offspring:

$$\begin{bmatrix} MF(\tilde{\mathbf{s}}_1') & \mathbf{i}_1' \\ MF(\tilde{\mathbf{s}}_2') & \mathbf{i}_2' \\ \vdots & \vdots \\ MF(\tilde{\mathbf{s}}_{n/2}') & \mathbf{i}_{n/2}' \end{bmatrix} \quad (3-11)$$

6. The current part now serves as parents. For simplicity purposes, consider the two parents to be:

$$\begin{aligned} parant_1 &= [\mathbf{i}_1' \quad \mathbf{i}_2' \quad \cdots \quad \mathbf{i}_{n/4}'] \\ parant_2 &= [\mathbf{i}_{n/4}' \quad \mathbf{i}_{n/4+1}' \quad \cdots \quad \mathbf{i}_{n/2}'] \end{aligned} \quad (3-12)$$

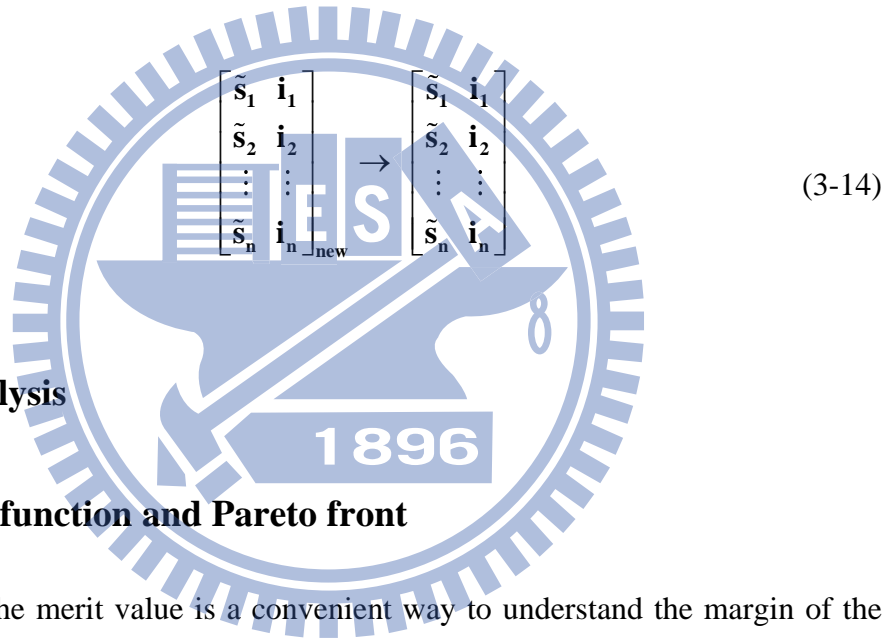
In the mating step, the crossover current vectors are randomly selected, and then the currents in between these vectors are merely swapped between the two parents. For example, if \mathbf{i}_1' and $\mathbf{i}_{n/4+1}'$ are two vectors that have been randomly chosen, their offspring can be a simply generated by:

$$\begin{aligned} (\mathbf{i}_1')_{\text{new}} &= \mathbf{i}_1' - \beta(\mathbf{i}_1' - \mathbf{i}_{n/4+1}') \\ (\mathbf{i}_{n/4+1}')_{\text{new}} &= \mathbf{i}_1' + \beta(\mathbf{i}_1' - \mathbf{i}_{n/4+1}') \end{aligned} \quad (3-13)$$

where β is a random number within the interval $[0, 1]$.

7. The problem with the crossover method is that no new information is introduced. It can be solved by multiplying a certain mutation rate, i.e. 10%, into the total number of drive currents, which is able to avoid the predicament of overly fast convergence or trapped at a local limitation.

8. Finally, the new offspring (current combinations) and their spectra are regarded as the new initial population to substitute the original one. The described process is iterated for several generations until the convergence requirement is satisfied.



$$\begin{bmatrix} \tilde{s}_1 & \mathbf{i}_1 \\ \tilde{s}_2 & \mathbf{i}_2 \\ \vdots & \vdots \\ \tilde{s}_n & \mathbf{i}_n \end{bmatrix}_{\text{new}} \rightarrow \begin{bmatrix} \tilde{s}_1 & \mathbf{i}_1 \\ \tilde{s}_2 & \mathbf{i}_2 \\ \vdots & \vdots \\ \tilde{s}_n & \mathbf{i}_n \end{bmatrix} \quad (3-14)$$

3.4 Merit analysis

3.4.1 Merit function and Pareto front

The analysis of the merit value is a convenient way to understand the margin of the system. The main spirit can be elaborated by a system used for general lighting. In the beginning, a purpose-oriented merit function MF (or called objective function) shall be proposed. Here we define MF , based on the weighted sum method ^[53], with two figures of merit: luminous efficiency (LE) and color quality scale (CQS), respectively:

$$MF = w \times CQS + (1 - w) \times LE, \text{ subject to } w \in [0,1] \quad (3-15)$$

where CQS is a refined color quality index of CRI (please refer to Appendix I). The weight factor w provides an additional degree of freedom for users to determine the

operation point among different figures of merit in accordance with different operational circumstances. Nevertheless, the prescribed condition is only valid when the profile of the two-dimensional optimal boundary (Pareto front, PF), with respect to CQS and LE , has been completed, which indicates that the system needs to be continuously optimized for a series of weight factor w . Furthermore, the changes of the initial environment (i.e. ambient temperature) and the target chromaticity point will produce separate PF that has to be regenerated. Due to this laborious calculation, we hereby proposed two sampling methods SA_1 and SA_2 , to improve the computational efficiency and costly analyze the cluster performance among figures of merit as well. The concept of the sampling in the merit analysis is intrinsically similar to the aberration analysis by sampled fields of view (usually at object height of 0, 0.5, 0.7, and 1) in lens design^[54].

3.4.2 Sampling method SA_1

Figure 3-4(a) shows three classical cases that users might encounter in merit analysis. The solid curved Pareto fronts PFs generated by SA_1 are aimed for separate target color temperature CT_1 , CT_2 and CT_3 , respectively. The first step of SA_1 is to preliminary examine the locations of both extreme points $P_0(CQS_0, LE_0)$ with $w = 0$ and $P_1(CQS_1, LE_1)$ with $w = 1$, where P_0 represents the efficiency mode that all the weight is attributed toward LE , and P_1 thus represents the quality mode associated with all weighting CQS . Either end P_0 or P_1 located at quadrant III will lead to the failure in satisfying the user-defined specification (quadrant I, defined by the minimum luminous efficiency LE_m and minimum color quality scale CQS_m). The reason is due to the optimal boundary would always exhibit a tradeoff relation and not likely to appear positive slope. If the condition of the Pareto front locus is partially qualified such as PF_1 or PF_2 , another two points P_a and P_b with random selected

weights a and b will be calculated to help us success in numerical connecting relations, via a cubic function, between (a) $CQS - LE$, (b) $CQS - w$, and (c) $LE - w$ of the optimal boundary.

We take PF_2 as an example to show the use of these relations. Presently the modeled curve partially overlaps with quadrant I defining an operation portion (red curve) with two extreme ends, whose weights w_{Cm} and w_{Lm} can be estimated by imposing CQS_m into the $CQS - w$ cubic function and bringing LE_m into the $LE - w$ cubic function, respectively. As a consequence, an appropriate weight $w_{Lm} < w < w_{Cm}$ could be obtained from the proposed sampling method SA_1 with a small number of sample points. The procedure of SA_1 is summarized in Figure 3-4(b).

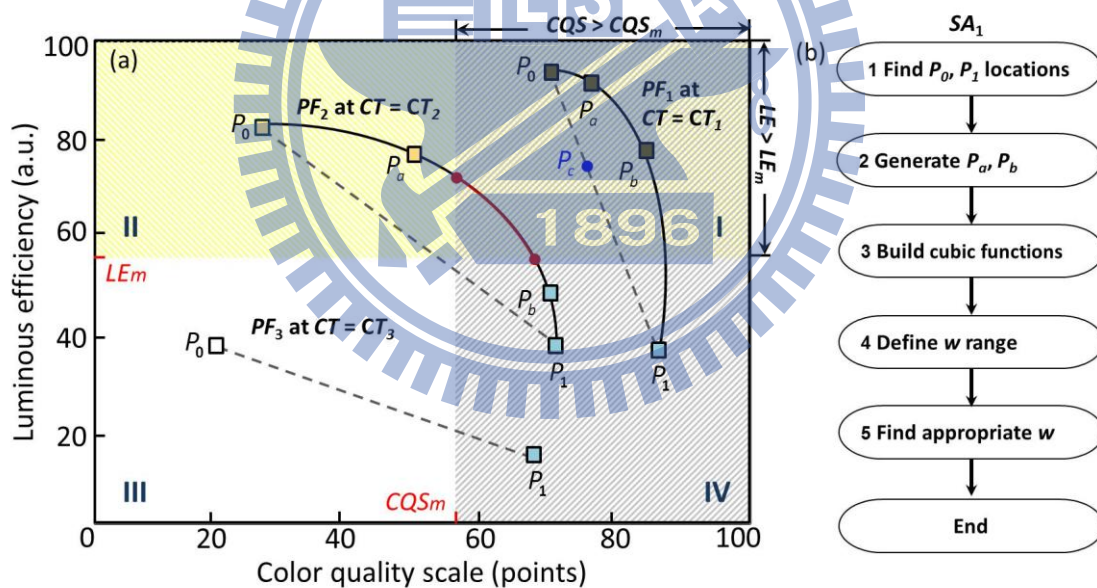


Figure 3-4 (a) The illustration of the Pareto fronts PFs for different CTs on the $CQS - LE$ plane. (b) The flowchart of SA_1 . Either end point P_0 or P_1 located within quadrant III will lead to an unacceptable performance as PF_3 . The curve with end points located within quadrant II and IV, like PF_2 , should be confirmed the operation portion (red curve).

3.4.3 Sampling method SA₂

Compared with the sampling method SA₁, linear approximation is computationally efficient to determine the appropriate operating point, shown as the dash lines in Figure 3-4(a). In this way, we only consider the case that the line $\overline{P_0P_1}$ has crossed quadrant I such as PF_3 . For no good reason, we choose P_0 (highest LE mode or efficiency mode) as the starting point, the increment rate of CQS ($CQS_{1/0}$) at expense of LE decrement ($LE_{1/0}$) can be defined as:

$$\begin{aligned} CQS_{1/0} &= \frac{CQS_1 - CQS_0}{CQS_0} \\ LE_{1/0} &= \frac{LE_1 - LE_0}{LE_0} \end{aligned} \quad (3-16)$$

For an arbitrary point $P_c (CQS_c, LE_c)$ located on the line $\overline{P_0P_1}$, the corresponded weight c can be determined by:

$$c = \frac{(CQS_c - CQS_0) / CQS_0}{CQS_{1/0}} = \frac{(LE_c - LE_0) / LE_0}{LE_{1/0}} \quad (3-17)$$

where c also indicates the increasing rate of $CQS_{1/0}$ as well as the decreasing rate of $LE_{1/0}$. The linear approximation method SA₂ is a fast way to find the optimal operating point without evaluating additional points, while the cost is the less precise estimation in weight value. Moreover, this method might face risk as the case of PF_2 that the real Pareto front cross quadrant I but $\overline{P_0P_1}$ doesn't.

3.5 Judgment

So far, a multispectral system has been optimized for certain initial circumstances with an appropriate weight value w . However, during the course of spectral synthesis, as a situation that one LED is dimming to an extremely low level, we can possibly remove it without affecting the system performance. Likewise, we can add the number of LEDs to allow the operation in adequate margin. Either scheme has a good correspondence with the skills the lens design used as follows ^[55]:

1. Among the operating wavelengths, add a new available wavelength and vary its emission power to analyze the merits (*CQS* and *LE*) again. It is usual to insert a wavelength at the large interval between peak wavelengths.

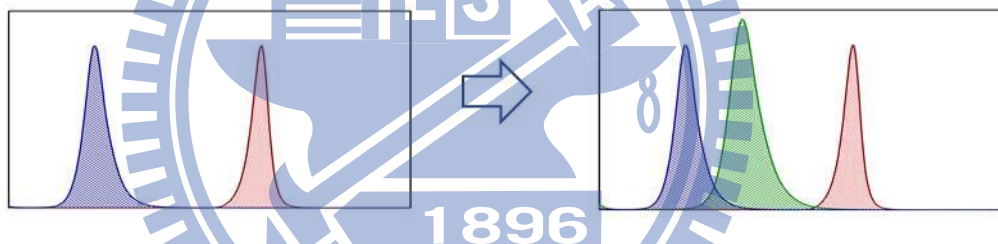


Figure 3-5 A green wavelength inserted at the large wavelength interval.

2. Replace two or more single-colour LEDs by a phosphor-converted LED, or vice versa. If there is a remarkable performance advance in any kind of LEDs, try to adopt it.

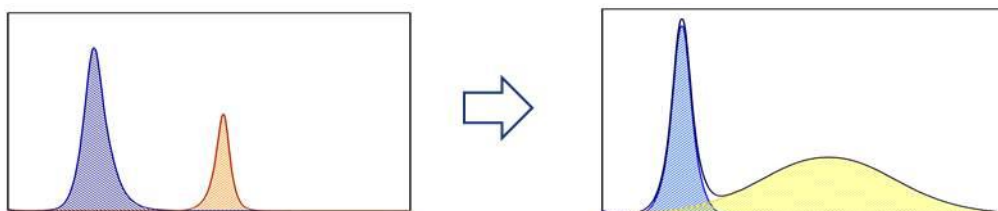


Figure 3-6 Two or more single-colour spectrum replaced by a phosphor-converted source.

3. Split an operating wavelength of too-high emission power into two adjacent wavelengths. This may be useful to avoid the dangerous operation in tiny margin of the requirements.

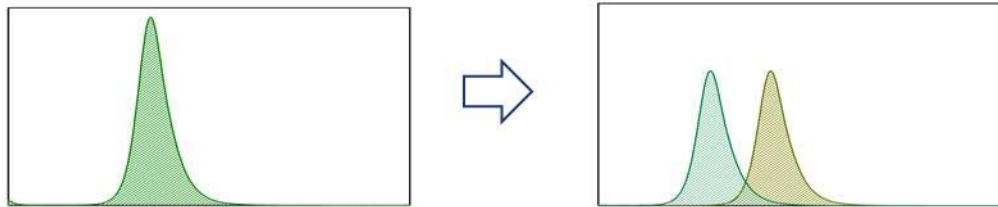


Figure 3-7 An operating wavelength of too-high emission split into two adjacent wavelength.

Once the optimal boundary crosses the user-defined specification (quadrant I), we can fix an appropriate weight value by using SA_1 or SA_2 for the merit function accordingly.

3.6 Tolerance analysis

Finally, the designer can sequentially introduce a small perturbation to each parameter ($\hat{\lambda}$, $\Delta\lambda$, I_{DC} , T_a) and observe the corresponding change. It is noted that the presented technique merely confine the discussion to the spectral range, it is not likely to predict the light field changed by the geometric deviation such as LED package error or assembly misalignment. A possible compensation mechanism which constantly measures the SPD on the illuminated plane and gives feedbacks to drive currents might be helpful to tolerance the LED cluster ^[10].

3.7 Summary and conclusions

A novel LED mixing scheme analogous to the conventional lens design process has been proposed. The algorithm enables the users to easily determine the optimal LEDs set to meet the requirements such as light efficiency, color quality, or other figures of merit over a wide range of color temperature. The procedure includes six steps: (3.1) initial system, (3.2) define boundary condition, (3.3) optimization, (3.4) merit analysis, (3.5) judgment, and (3.6) tolerance analysis, and each step has been carefully considered in turn.

We list three suggestions for initial system to pick appropriate LED set from the “LED map”. After that, domains of input variables (i.e. the drive current I_{DC} and ambient temperature T_a) and the additional confinement (e.g. $\Delta xy < 0.01$) should be predefined before going through optimization process. To obtain the optimal composite spectrum, a globe searching engine, continuous genetic algorithm CGA has been adopt with eight iterative processes in Figure 3-3. Based on the user-defined merit function, we correspondingly proposed two sampling methods SA_1 and SA_2 , to improve the computational efficiency and costly analyze the cluster performance among figures of merit. For the system is under qualified, three skills presented in Section 3.5 may allow the operation in adequate margin. Finally, with a small perturbation to each parameter, the tolerance of the optimized system can be observed.

Chapter 4

Applications of the Multispectral Mixing Scheme

4.0 Goal

The proposed mixing scheme in previous chapter theoretically provides more efficient optimization for multispectral LEDs clusters than is provided by previous researchers. In this chapter, we realize the mixing scheme into two examples individually adopting (1) low power LEDs cluster and (2) high power LEDs cluster. Both of them are planned for general lighting use. Therefore, they share the same merit function MF that is identical to Equation (3-15), where the merits of figure composed of color quality scale CQS and luminous efficiency LE are linearly combined by weighted sum method. For the low power LEDs case, the objective is to demonstrate how a LEDs cluster with high luminous efficiency (LE is 97% of cluster's theoretical maximum value) and high color quality scale ($CQS > 80$ points) can be generated by following the devised methodology step-by-step. After that, we aim to release the constraint of the constant ambient temperature on LEDs system and extend the thermal operation window for the high power LEDs case. The result shows that the proposed method is experimentally validated to offer a full operable range in ambient temperature (T_a from 10° to 100°C) associated with high CQS (above 85 points) as well as high LE (above 100 $lm/watt$).

4.1 Case 1: Low power LEDs cluster design

We setup a multispectral platform composed of four single-colour LEDs (Excellence Opto. Inc., EOQ-5ERF red, EOQ-5EYF amber, EOQ-5DFE green, EOQ-5EBF blue) and a phosphor-converted cool-white LED (Excellence Opto. Inc., EOQ-5EWF). The corresponded spectra at ambient temperature T_a of 25 °C and drive currents I_{PWM} of 20 mA are shown in Figure 4-1. An adequate layout of LED arrangement and optics with first-order design are considered to deliver a uniform illumination on the measured plane ^[56]. Due to the relative low level of drive currents (maximum 20mA) controlled by the pulse-width modulation (*PWM*) approach, the modeling of the spectral power distribution *SPD* for each colour LED can be assumed to satisfy the scalability and additive property in color mixing scheme ^[57], which indicates the *SPD* can be thermal-independent and be regularly proportional to drive currents without distortion.

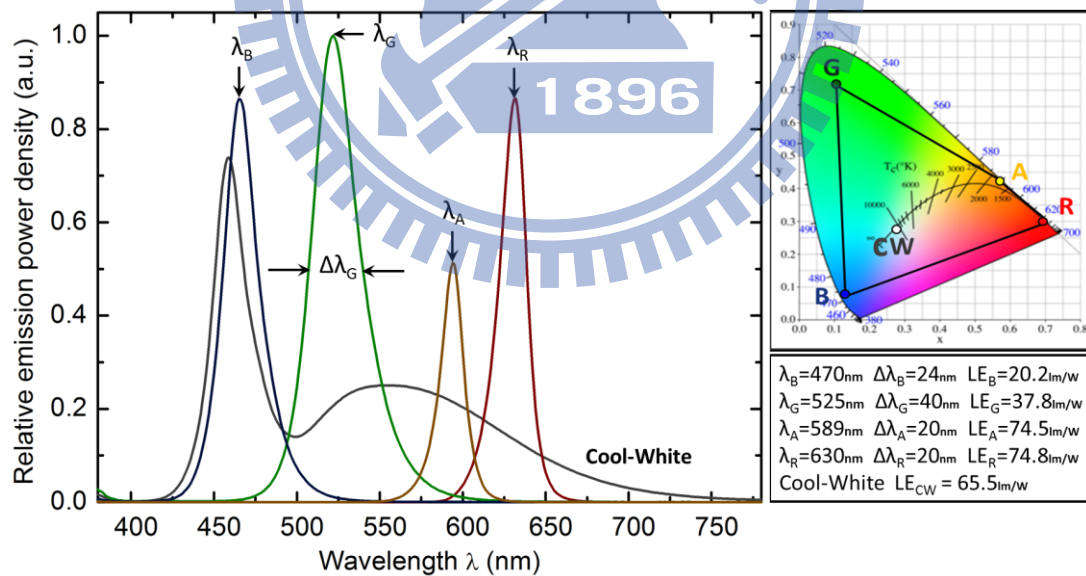


Figure 4-1 The spectra of red (R), green (G), blue (B), amber (A) and cool-white (CW) LEDs at ambient temperature T_a of 25 °C with all drive currents of 20 mA. The corresponded chromaticity points and specifications are also shown in the figure. The drive currents controlled by PWM approach have the pulse width of 6.66 ms at differences of 0.04 ~ 0.06 ms for each gray level (a total of 128 gray levels).

4.1.1 Validation of the composite spectrum

As the aforementioned process, we start to fulfill the models of multispectral LEDs through optimization step with weight factors $w = 0$ (efficiency mode) and 1 (quality mode). The resultant spectra for color temperatures $CT = 3000\text{K}$ and 6500K are selected to be verified as shown in Figure 4-2, where the simulations are in close agreement with the experimental measurements by checking the R^2 value (above 0.98) and the chromaticity deviation Δxy (below 0.01). The Figure 4-3 features illuminant environments for both color temperatures 3000K and 6500K at the efficiency mode. Apparently the appearance of the color checker chart is more accurate in the booth with higher CQS than that in the booth with poor CQS (refer to the difference of the grey scale coloured squares between these booths).

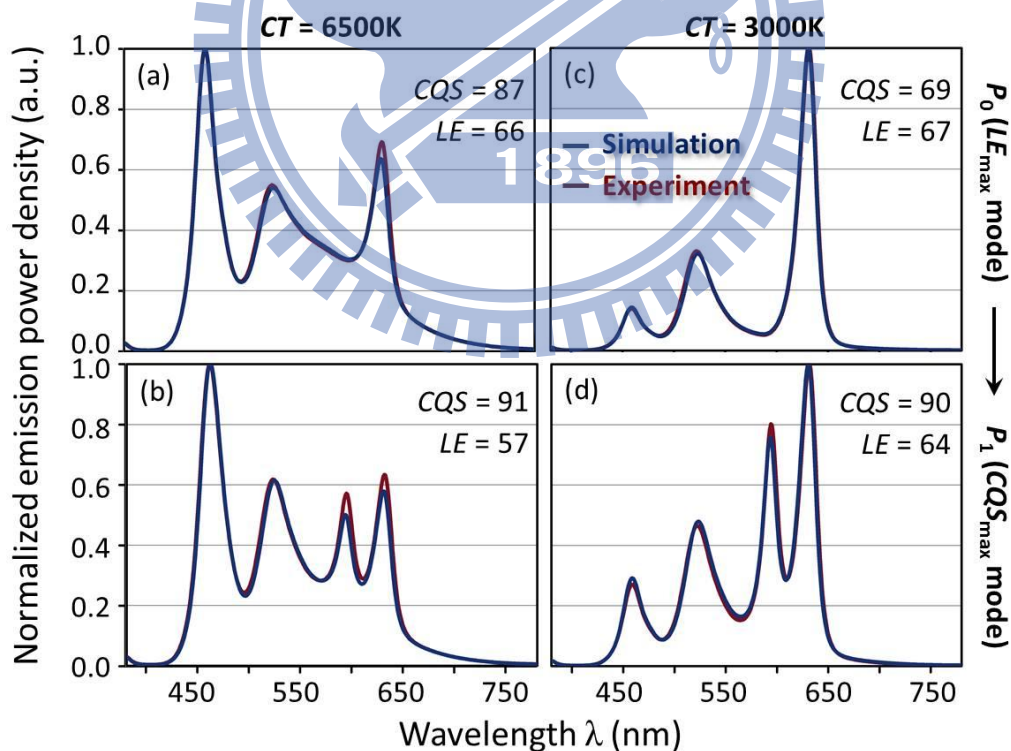


Figure 4-2 Spectral comparisons of simulations and experiments for P_0 and P_1 at CTs of 6500K and 3000K , respectively. The simulated spectra closely matched the measurements in spite of a few peak deviations.

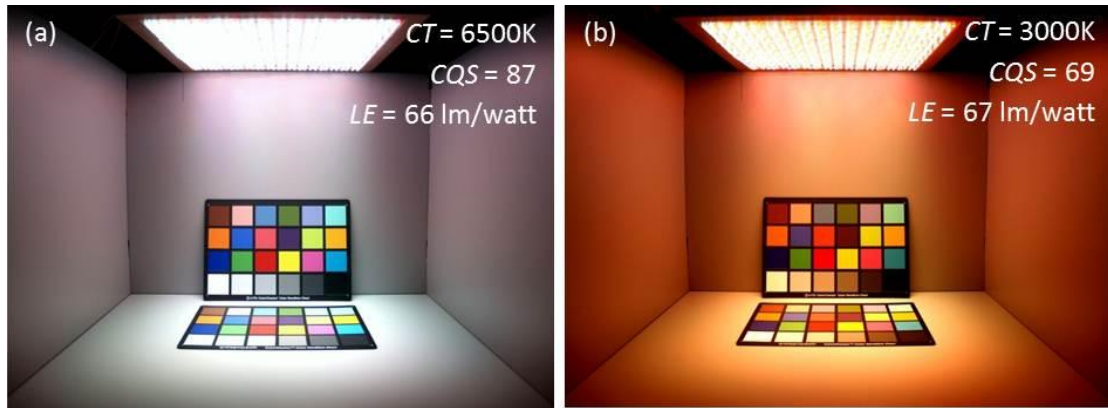


Figure 4-3 The illuminant environments at (a) P_0 ($CQS = 87$ points, $LE = 66$ $lm/watt$) for $CT = 6500K$ and (b) P_0 ($CQS = 69$ points, $LE = 67$ $lm/watt$) for $CT = 3000K$ show apparently different color rendering abilities.

4.1.2 Comparison of R/G/B and R/G/B/A system

In addition to the experimental validation, more insight can be pursued by the quantitative analyses. Here we assume the minimum requirements for color rendering $CQS_m = 80$ points and luminous efficiency $LE_m = 60$ $lm/watt$. Based on the linear approximation SA_2 method, the loci of R/G/B, R/G/B/A, and R/G/B/A/CW are presented in Figure 4-4. The black curve in Figure 4-4(a) depicts the referenced single solution of R/G/B cluster for color temperature CT from 1000K to 10000K. It can be noted that all of the solutions are far from the required performance (quadrant I). We then add the amber (A) source to the R/G/B cluster, the average improvement of 50% in color quality scale CQS is achieved without too much loss of luminous efficiency ($LE_{1/0} < 5\%$). This result is generally in accordance with the concept that the color rendering performance of sources would be improved when its modulated spectrum is as smooth as sunlight.

For the solution of each color temperature CT , the point P_0 ($w = 0$) is set as the starting point as we mentioned in the Section of merit analysis. In the view point of P_0 , the information of the increment rate of CQS denoted as $CQS_{1/0}$ and the sacrifice of

decrement rate of LE denoted as $LE_{1/0}$ can be given in Figure 4-5. The result of the R/G/B/A case shows that all circle points for whole range of color temperature CT are located at right-top corner. Thus the designer would undoubtedly chose a high weight value ($w \sim 1$) to boost the color rendering ability with a little expense of cluster efficiency. This tendency is equivalent to drive P_0 to approach P_1 along the straight line in Figure 4-4 (a). Nevertheless, the R/G/B/A cluster still suffers a stringent operating window of CT from 2800K to 3000K, which would strictly preclude its use in intelligent lighting applications.

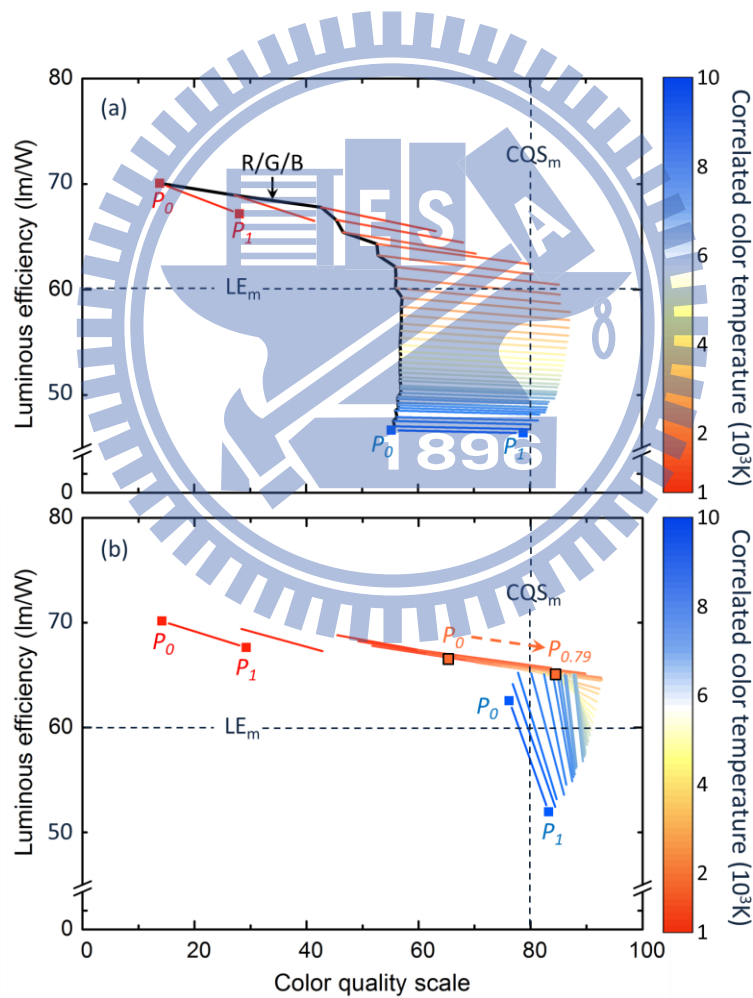


Figure 4-4 The SA_2 results of (a) R/G/B (black curve), R/G/B/A, and (b) R/G/B/A/CW clusters aimed to P_1 and P_0 for full range of CT from 1000K to 10000K.

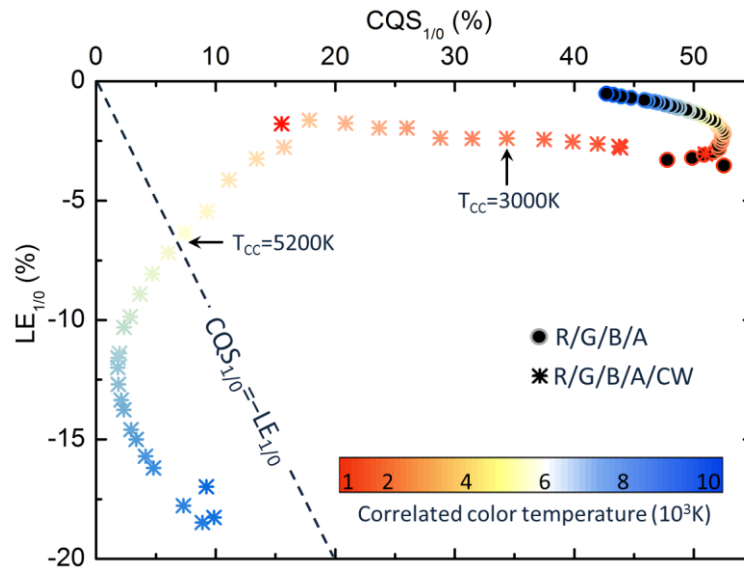


Figure 4-5 The results of $CQS_{1/0}$ and $LE_{1/0}$ for R/G/B/A and R/G/B/A/CW clusters. By using SA_2 analysis, R/G/B/A/CW can further extend the operation window in color temperature.

4.1.3 The effect of cool-white LED

Compared with the R/G/B/A cluster, the addition of cool-white (CW) LED is able to further extend the operational window throughout the entire color temperature range. To prove this statement we can select a start point P_0 at $CT = 3000K$, whose $CQS_0 = 66.8$ points (unqualified) and $LE_0 = 66.7$ $lm/watt$ [refer to Figure 4-4 (b)]. The corresponded information of $CQS_{1/0} = 34.3\%$ and $LE_{1/0} = -2.4\%$ at the same point P_0 can be found in Figure 4-5. With above parameters, it is readily to derive an appropriate weight of 0.79 by using Equation (3-17) to fulfill the requirement, where the CQS value is increased to 85 points at the expense of 1.3 $lm/watt$.

Generally, the weighting value can be conducted to the comparison between $CQS_{1/0}$ and $LE_{1/0}$. That means the balance condition of $CQS_{1/0} \approx -LE_{1/0}$ at color temperature CT of 5200K (Figure 4-5) could be regard as a turning point for the weight selection. By applying this weight value selection strategy to the R/G/B/A/CW combination, it is logically to choose a large weight value ($w > 0.5$) for $CT < 5200K$

and vice versa in order to approach the requirements. In sum, adapting the phosphor-converted white source could further increase 5% in CQS and 20% in LE over full range of color temperature, which is due to the cool-white LED associated with high efficiency offers a good candidate to substitute the function of blue colour. The detail will be analyzed as follows the illustration of Figure 4-6.

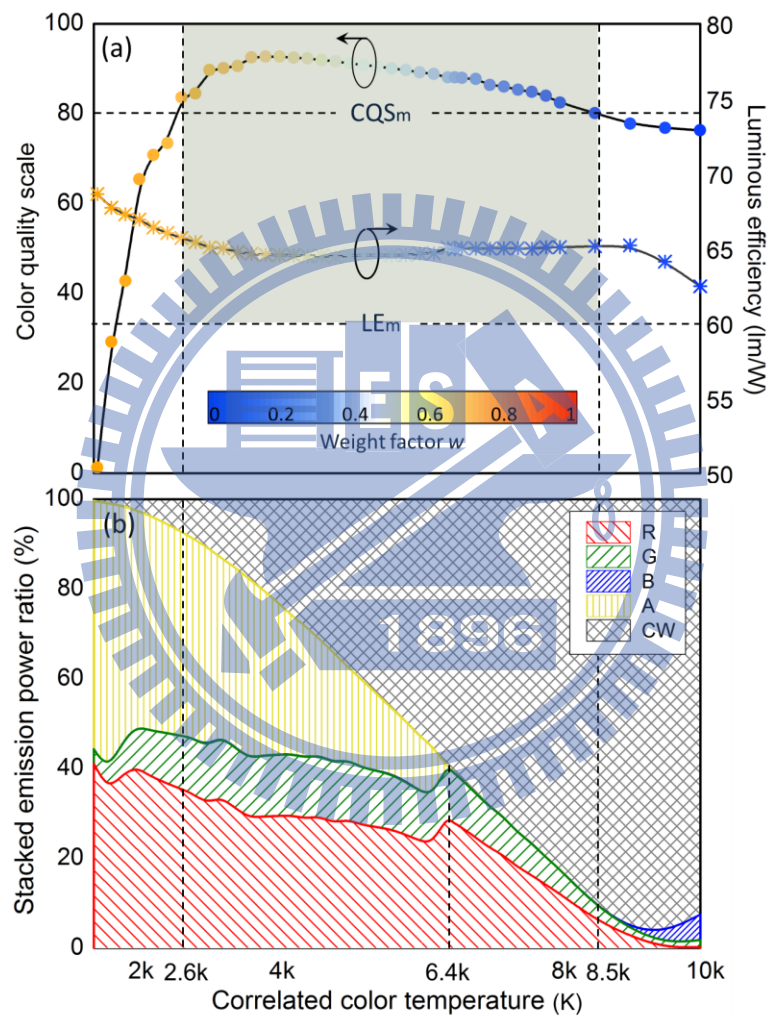


Figure 4-6 (a) The values of CQS and LE , and (b) the stacked emission power ratio versus color temperature for the optimized R/G/B/A/CW design ($CQS_m = 80$ points and $LE_m = 60$ lm/watt). The operation window has been extended to $2600K < CT < 8500K$ with the selected weight via SA_2 selection method. It is noted that the operation window is mainly restricted by the CQS due to the correction factor at the extreme color temperature.

4.1.4 The color tunable R/G/B/A/CW system

At this point, we can successfully determine the operation point by the proposed methodology and set an optimal lighting environment for R/G/B/A/CW system. As shown in Figure 4-6, the operation window is extended to span across 2600k – 8500K with the user-defined requirements of $CQS_m = 80$ points and $LE_m = 60 \text{ lm/watt}$, which would be shrink by more severe lighting requirement accordingly (e.g. the operation window of 3200 – 5600K for $CQS_m = 90$ points and $LE_m = 64 \text{ lm/watt}$).

Based on Figure 4-6, we can find that when the color temperature is less than the 6400K, the power ratio is mainly governed by the light quality requirement, and each component has a comparable amount. On the other hand, the efficiency requirement is dominated and contributed by cool-white LED when the operation temperature is higher than 6400K. The combination of LED cluster reduces to R/G/CW for $6400\text{K} < CT < 8500\text{K}$ as shown in Figure 4-6 (b). Within the operation window of 2600K – 8500K, the function of blue LED has been replaced by the cool-white light source, so that we can discard it from the cluster for most general lighting applications.

4.2 Case 2: High power LEDs cluster design

In the high power multispectral mixing, the thermal issue is no longer independent but should be included in spectrum prediction as we modeled in Chapter 2. In contrast to low power design, in this section we setup another pentachromatic mixing platform, where a high-power LEDs cluster is composed of four single-colour LEDs (HELIO Optoelectronics Corp., HMHP-E1HR red, HMHP-E1HA amber, HMHP-E1HG green, HMHP-E1HB blue) and a phosphor-converted HMHP-E1HW white LED. Figure 4-7 shows the spectral power distribution *SPD* of each channel under operational condition $T_a = 10 \text{ }^\circ\text{C}$ and $I_{DC} = 350 \text{ mA}$, respectively. An adequate

layout of LED pixel arrangement and first-order design delivers a uniform illumination upon the test Macbeth color checker ^[56].

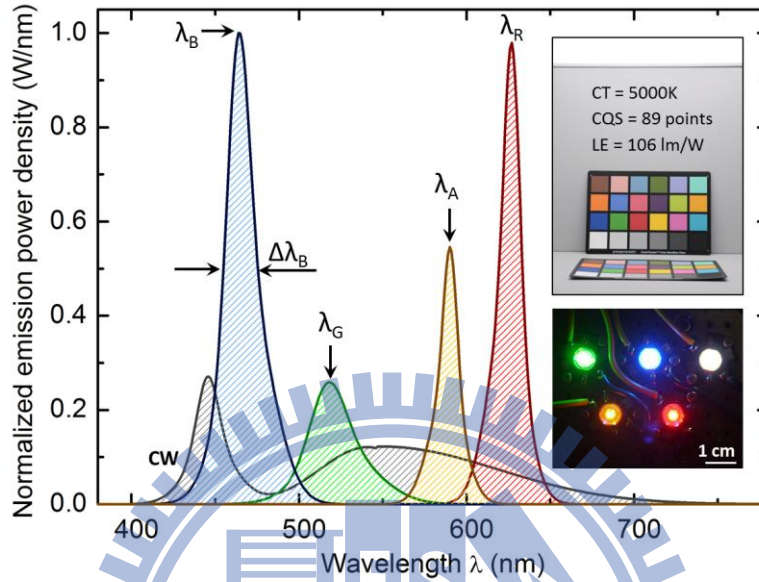


Figure 4-7. The power spectra of red (λ_R : 625nm, $\Delta\lambda_R$: 20nm), green (λ_G : 523nm, $\Delta\lambda_G$: 33nm), blue (λ_B : 465nm, $\Delta\lambda_B$: 25nm), amber (λ_A : 587nm, $\Delta\lambda_A$: 18nm) and cool-white LEDs at T_a of 10 °C with I_{DC} of 350 mA. The upper right figure shows a real-field test designed for $CT = 5000K$ and the lower right one shows the utilized LEDs attached on the temperature controllable fixture respectively.

4.2.1 The influence of ambient temperature on color mixing

The first validation of the devised model is conducted by examining the temperature dependence of spectra under four color temperatures: $CT = 3200K, 4600K, 6200K,$ and $7400K$, respectively. The system is operated under a specific value of the ambient temperature, $T_a = 50$ °C. The results are reported in Figure 4-8, where the illumination conditions fulfill the requirements of high luminance level (100 lm), negligible color deviation ($\Delta xy < 0.01$) and high quality ($CQS > 85$ points) with possibly highest luminous efficiency LE . If we change the ambient temperature without compensation, the lighting performance would dramatically shift due to the thermal effects. Taking

$CT = 3200\text{K}$ for example, as ambient temperature increases from 10°C to 100°C , the chromaticity point would have an apparent change ($\Delta xy > 0.5$). On the other hand, in case of settled operational ambient temperature $T_a = 50^\circ\text{C}$, the acceptable tolerance ($\Delta xy < 0.01$) of thermal dependence merely lie in a tiny window $T_a = 42^\circ\text{C} \sim 56^\circ\text{C}$. It is observed that the operational window changes with respect to different chromaticity points. The drift of chromaticity point subject to thermal dissipation becomes more severe at low CT , which is mainly attributed by amber and red color. The reason can be explained by Figure 4-9.

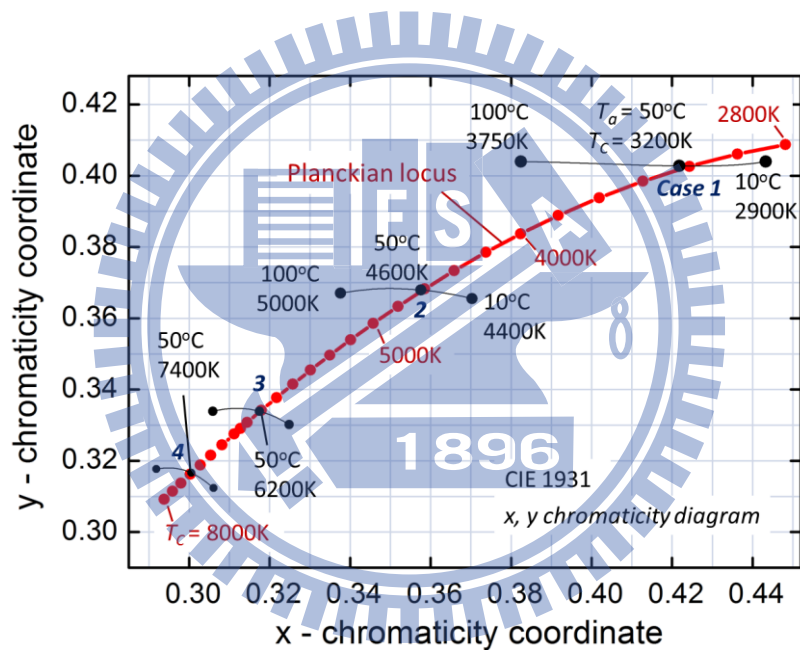


Figure 4-8. The temperature dependence of spectra designed for $CT = 3200\text{K}$, 4600K , 6200K , and 7400K at $T_a = 50^\circ\text{C}$. The chromaticity point shifts toward higher color temperature with the raise of T_a owing to the dramatic deterioration in LEs of the red and amber LEDs.

When the ambient temperature T_a increases to 100°C , luminous efficiencies (LEs) of amber and red LED suffer from 23% and 46% decreases of those at 10°C , respectively. The results is in agreement with the previous literature, experimentally validated the output power decreases by increasing ambient temperature [58]. This

phenomenon can be attributed to two reasons: (1) In viewpoint of spectral characteristics, the *SPDs* of amber and red color would shift to longer wavelength at high ambient temperature T_a , resulting in the decreases of luminous efficiency [32]. (2) In terms of material, for the AlInGaP-based LEDs, due to the carrier overflow by increased ambient temperature, the luminous efficiency would be reduced accordingly [58].

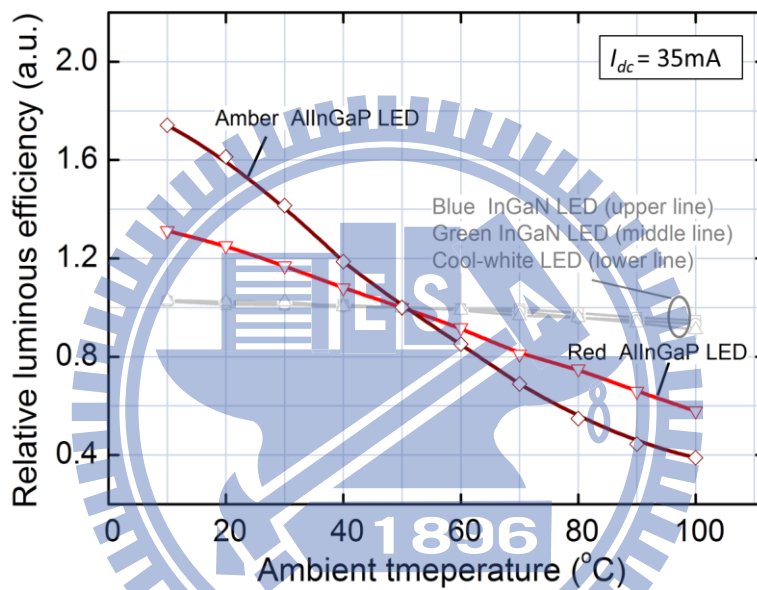


Figure 4-9. The temperature dependence of LE for pentachromatic LEDs. When T_a is varied from 10 °C to 100 °C, LEs of amber and red AlInGaP LEDs decrease to 23% and 46% of that at 10 °C while LEs of InGaP LEDs are insensitive to temperature variation.

4.2.2 Spectral modulation with thermal compensation

In order to compensate the drift caused by thermal effects, the proposed optimization methodology shall be applied to different ambient temperatures in the first place. Thus a table of drive current versus ambient temperature can be preloaded to the cluster system for practical operation. Table 4-1 shows the example that summarizes the compensation outcomes for the extreme T_a of 10 °C and 100 °C.

Table 4-1. The comparison of CQS , LE , output luminous flux Φ_v , correlated color temperature CCT , color temperature CT and the input power ratio P_{in} under $T_a = 10^\circ\text{C}$, 50°C and 100°C .

	Case	1	2	3	4
10°C	$CCT(K)$	2900	4400	6100	7300
	CQS	86	89	87	86
S_1^*	$LE (lm/W)$	123	131	130	127
	$\Phi_v (lm)$	127	114	110	109
	$CT (K)$	3200	4600	6200	7400
	CQS	89	91	90	88
S_2^{**}	$LE (lm/W)$	127	131	130	127
	$\Phi_v (lm)$	100	100	100	100
	$P_{in} (%)$	28:24:0:26:22	14:17:3:24:42	7:12:8:21:52	5:10:12:20:53
		R:A:G:B:CW			
M^{***}	$CCT (K)$	3168	4538	6145	7327
	CQS	88	90	89	88
	$LE (lm/W)$	124	128	128	125
	$\Phi_v (lm)$	96	97	96	96
50°C	$CT (K)$	3200	4600	6200	7400
	CQS	90	89	89	87
S_1^*	$LE (lm/W)$	109	123	124	123
	$\Phi_v (lm)$	100	100	100	100
	$P_{in} (%)$	33:23:0:23:21	17:17:2:21:43	5:12:7:18:58	5:9:11:16:59
	$CCT (K)$	3226	4631	6170	7365
M^{***}	CQS	88	88	87	86
	$LE (lm/W)$	105	118	120	120
	$\Phi_v (lm)$	95	94	96	95

	<i>CCT</i> (K)	3750	5000	6600	7700
100°C	<i>CQS</i>	77	86	87	87
	<i>LE</i> (lm/W)	82	103	111	110
S_1^*	Φ_v (lm)	74	84	88	89
	<i>CT</i> (K)	3200	4600	6200	7400
	<i>CQS</i>	87	87	87	87
S_2^{**}	<i>LE</i> (lm/W)	62	92	109	107
	Φ_v (lm)	100	100	100	100
	P_{in} (%)	44:24:0:18:14	11:28:1:19:41	1:15:3:11:70	1:12:9:12:66
	<i>CCT</i> (K)	3252	4687	6253	7439
M^{***}	<i>CQS</i>	86	85	86	86
	<i>LE</i> (lm/W)	59	87	105	104
	Φ_v (lm)	95	95	95	97

* Simulation without compensation

** Simulation with compensation

*** Measurement result

It is observed that the technique effectiveness is fully applied for the predefined requirements in smart lighting: high color quality scale (above 85 points), high luminous efficiency (above 100 lm/watt) over a wide range of color temperature ($CT = 2800-8000K$). The thermal compensation technique works with wide chromaticity locus and, in particular, it is proven to work with low color temperature noticeably influenced by thermal variation. Taking case I ($CT = 3200K$) as an example, as the ambient temperature T_a changes from 10 °C to 100 °C, the power ratio of dominant red channel changes from 28% to 44%. This modulation is predictable because the decreased luminous efficiency LE of the dominant field (red color) follows the raise of the ambient temperature. In order to keep the chromaticity point, we must extract more luminous flux from the red majority and thus more power ratio (P_{in}) is required accordingly.

The consequence can be deduced in other operational conditions. As the lighting is operation at high color temperature ($CT > 4600K$), phosphor-converted white source is the dominant field (over 50%) due to its unique characteristics of high luminous efficiency and dully dependence upon the thermal effects. Therefore, in case of operation in high color temperature (CT), we suggest a scenario as following: (1) utilize phosphor-converted white source as a dominant field, accompanied by a small amount of other complementary single-color to keep the light quality and the adjustable chromaticity, (2) replace single red or amber emitter by two or more devices with less drive current, and thus reduce the thermal effect and enhance the entire cluster efficiency, (3) replace amber AllnGaP LED by phosphor-converted amber with higher flux density and better color stability ^[59].

4.2.3 Optimized pentachromatic LEDs cluster

In sum, Figure 4-10 shows the contour map of possibly highest luminous efficiency LE subject to predefined requirements ($CQS > 85$ points, high luminance level 100 lm and negligible color deviation $\Delta xy < 0.01$). With different operational ambient temperatures, it's not likely to reach high efficiency at high ambient temperatures. The best performance ($LE > 130\text{ lm/watt}$) lies in a narrow region about $CT = 4000 - 6500K$ associated with self-evident low ambient temperature ($T_a = 10^\circ C \sim 20^\circ C$). If the luminous efficiency $LE = 100\text{ lm/watt}$ is settled as the minimum requirement, a full operable range for ambient temperature T_a can be workable only within the high color temperature range $CT > 5200K$.

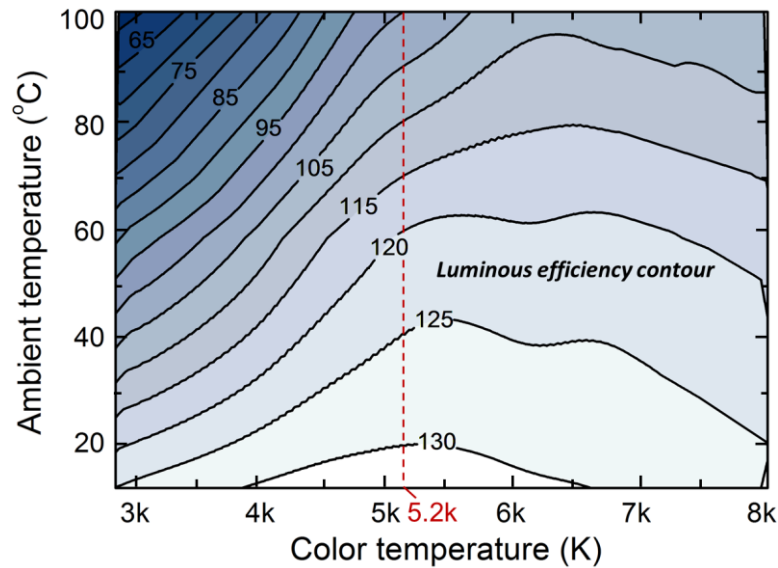


Figure 4-10. The LE contour of the pentachromatic LEDs cluster is performed under the predefined requirements ($CQS > 85$ points, lighting level = 100 lm and $\Delta xy < 0.01$). When the $LE = 100$ $lm/watt$ is selected as the minimum efficiency boundary, a full operation range for ambient temperature can be obtained for $CT > 5200K$.

4.3 Summary and conclusions

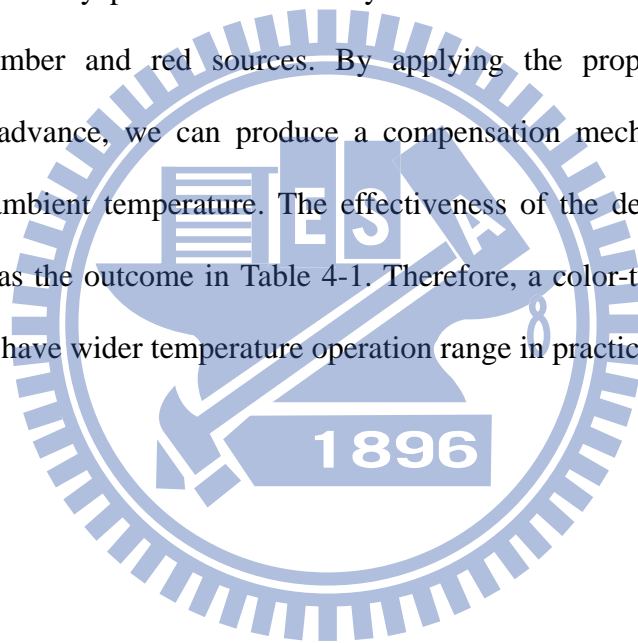
The proposed multispectral mixing scheme has been individually realized into two examples aimed for general lighting application. In the case of low power LEDs cluster, the SPD can be assumed to be thermal-independent. The composed spectra have been experimentally verified for different color temperatures and operation modes.

According to the comparison of the R/G/B and R/G/B/A system, we found that the system including amber source could have the average improvement of 50% in color quality scale CQS could without too much loss of luminous efficiency LE . In addition, it is better to operate the R/G/B/A cluster at the high color rendering mode (i.e. the weight factor ~ 1) with the analyzed result of $CQS_{1/0}$ and $LE_{1/0}$, while the

stringent operable range in color temperature still preclude its use in general lighting.

A hybrid design has therefore been proposed. The addition of cold-white (CW) LED to R/G/B/A system enables a further improvement to both *CQS* and *LE*, leading to an extended operation window from 2600K to 8500K. Thus a low power color tunable system can be accomplished.

For the case of high power LEDs cluster, the thermal effect and its influence on the chromaticity point have been analyzed. With the raise of the ambient temperature, the drift of chromaticity point can be mainly attributed to the decreased luminous efficiencies of amber and red sources. By applying the proposed optimization methodology in advance, we can produce a compensation mechanism against the whole range of ambient temperature. The effectiveness of the developed technique has been proven as the outcome in Table 4-1. Therefore, a color-tunable high power LEDs cluster can have wider temperature operation range in practical use.



Chapter 5

Conclusions and Future Works

5.1 Conclusions

The conclusions for this dissertation research are summarized as follows:

5.1.1 LED Spectral Characterization

1. The characterization is aimed to obtain the dependence between the input digital count (or drive current) and the output spectral power distribution of a LED. Because the resistance of a LED is highly affected by the thermal effect, in the first part of the thesis, we conducted a sequence of measurements to obtain the data base of voltage-temperature dependence subject to different drive current.
2. With the sufficient amount of sampling measured data, we could have the relation of junction temperature with respect to DC drive current and ambient temperature, as developed by A. Keppens [Equation (2-6)]. In that case, we can easily save the computational complexity; all the input and corresponding variables can be attributed by a single parameter: drive current.
3. In order to estimate the behavior of spectral power distribution with the reduced dimension, we approximate the *SPD* by Gaussian fitting, where three parametric features: peak wavelength, intensity and spectral width are functions of drive current and ambient temperature, respectively. The resultant *SPD* can be

represented as a form of Equation (2-12). In terms of primary-based LED, a double Gaussian approximation is sufficient to estimate its SPD with high accuracy. On the other hand, for phosphor-based LED, the SPD of excitation source and phosphor shall be approximated by individual double Gaussian forms.

5.1.2 Multispectral Optimization as Lens Design Techniques

1. To optimize the SPD of a LED cluster according to different operational purposes, we proposed a novel methodology, which can be conceptually analogous to the general lens design rule that has long been developed in past few decades.
2. The proposed methodology is based on an assumption that the thermal status were kept in a uniform distribution within a small group of LEDs (Section 3.3). As the assumption is no longer satisfied in entire cluster platform, more complicated method shall be employed ^{[60], [61]}.
3. The third part of multispectral optimization is to determine the operational point subject to purposed figures of merit. For the weight factor $w = 0$, the operational point P_0 represents the efficiency mode, that means the merit figure are optimized toward the consideration of maximum luminous efficiency. The other extreme case, P_1 , would be the quality mode. Because there is a fundamental tradeoff between LE and CQS , the slope of $\overline{P_0P_1}$ is always negative, which means it is not likely to enhance both merits at the same time.

5.1.3 Applications of the Multispectral Mixing Scheme

1. The low power R/A/G/B/CW design was proposed. The high efficiency phosphor-based cool-white LED substitutes the function of blue colour over almost whole range of color temperature, leading to an extended operation window from 2600K to 8500K. Such hybrid design shows the potential in realization of the high efficiency and high quality system.
2. In the low color temperature range, the channels (red, amber, green and cool-white) contribute comparable amount to form a white light. As we increase the target color temperature, the phosphor-based white light will become more and more important, which eventually becomes the dominant after 6400K.
2. The high power pentachromatic cluster with the temperature compensation scheme was accomplished. At high ambient temperature T_a , the luminous efficiency would suffer from a severe deterioration at low color temperature. The main reason is due to the dominant fields, red and amber, are strongly dependent on thermal dissipation. In order to avoid such issue, we suggest the replacement of a single emitter by two or more ones, which are able to share the total luminous flux and reduce the thermal effect accordingly.
- 3 This technique still leaves much space open and clearly more research must be carried out to explore its potential in full- the first, price and volume of the cluster being the realization of a commercial available solution. The preliminary demonstration presented here, however, indicates that proposed multispectral mixing scheme could create a major breakthrough in the field of general lighting and spectral technologies.

5.2 Future works

5.2.1 Other applications

The LEDs clusters with the possibly highest light quality and luminous efficiency has been accomplished by successfully adopting the proposed multispectral mixing scheme. However, by modifying the figures of merit in the merit function MF (or called objective function), the spectral tunable LEDs systems can be extended to more lighting applications. For example, a merit function MF that gauges the similarity between the synthesized spectrum and the target spectrum can be written as:

$$MF = \frac{\tilde{\mathbf{s}}^T \mathbf{s} - N\tilde{S}_m S_m}{\sqrt{(\tilde{\mathbf{s}}^2 - N\tilde{S}_m^2)(\mathbf{s}^2 - NS_m^2)}} \quad (5-1)$$

where \tilde{S}_m and S_m denote the mean values of estimated spectrum and the target spectrum respectively. This equation simply uses the definition of correlation coefficient by correlating the estimated $\tilde{\mathbf{s}}$ with target \mathbf{s} .

With the change of the target spectrum \mathbf{s} in equation (5-1), a LEDs cluster could be used to emulate various commercial or standard illuminations, i.e. discharge lamps or CIE Standard Illuminant A. The cluster mimics the spectra of standard illuminations could not only save the maintenance cost for a wide variety of sources but also simplify the calibrations of photometers and colorimeters. In 2005, I. Fryc et al use the spectral tunable LEDs system in place of the Illuminant A for calibrations of photometers and colorimeters to reduce measurement errors ^[62]. S. W. Brown and B. C. Johnson, in 2003, also utilized the cluster with tunable spectrum to generate the distribution of the ocean blue color spectrum in order to improve the calibration accuracy of remote sensing instruments ^[63].

Nevertheless, the estimation of variant sources needs a large number of LEDs to cover the spectrum range as much as possible, which would take a lot of time in optimization step due to plenty of iterative calculations involved. The same conclusion could be found in ref. [61], in which the optimization algorithm is based on the gradient method ^[64]. In order to solve this issue, recently a novel and unique methodology, the reverse model, is proposed by our research group on the basis of principal component analysis PCA ^[65]. We will show in the following section that this method is fundamentally iteration free for the spectral estimation problem, so that the drive current for each LED channel can be immediately calculated once the target spectrum is determined. Consequently, the possible road for the future work is to develop a spectral tunable system to experimentally validate the feasibility of the proposed reverse model.

A schematic spectral tunable system is shown in Figure 5-1. The LED heads composed of multiple spectral LEDs are attached to the integrating sphere, which will be mounted on thermal-controllable plates and can be driven and controlled individually by the computer-controlled power supply. A detector-array spectro-radiometer and a photometer are used as monitoring devices to capture the radiometric and photometric outputs of the sources. The computer sending the calculated current signals to the power supply will receive the feedback form the spectroradiometer. Through this process, the feasibility of the proposed model can be checked by analyzing the deviation between the target spectrum and the synthesized one.

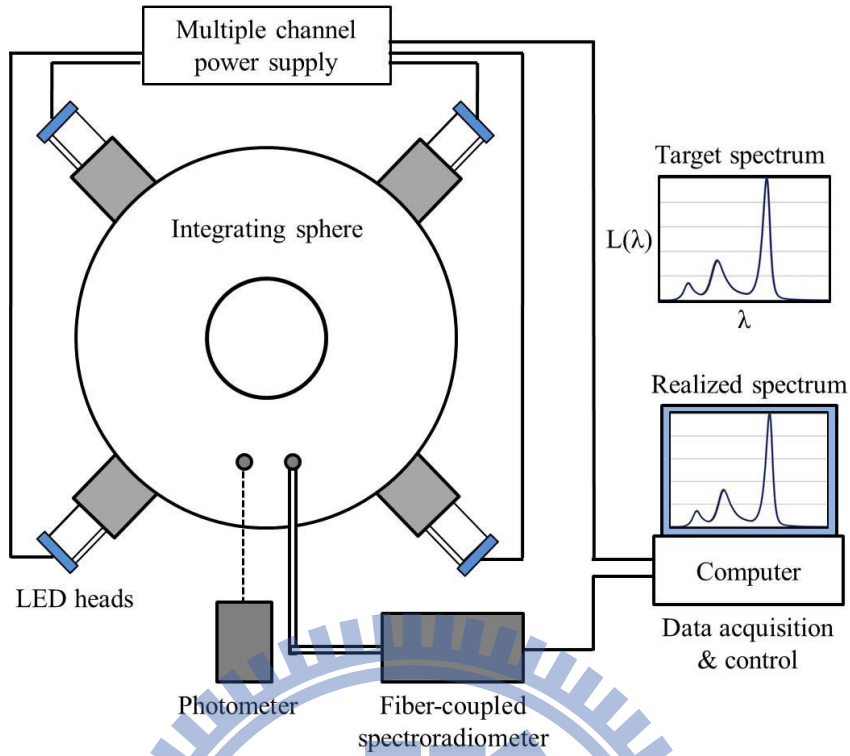


Figure 5-1 Configuration of the spectral tunable system [61].

5.2.2 Reverse model

As we have mentioned earlier, the reverse model is designed for the replacement of the iterative calculations. That indicates we still can stick to most of the design procedures introduced in Chapter 3 as well as the LED spectral characterization presented in Chapter 2. The schematic process is shown in Figure 5-2. Detailed mathematical treatment applied to each step will be described as follows:

1. First of all, we recall the initial synthesized spectral population $\tilde{\mathbf{S}}_p$ from Equation (3-7).

$$\tilde{\mathbf{S}}_p = [\tilde{\mathbf{s}}_1 \tilde{\mathbf{s}}_2 \dots \tilde{\mathbf{s}}_{m-1} \tilde{\mathbf{s}}_m]^T \quad (5-2)$$

Each row of $\tilde{\mathbf{S}}_p$, i.e. $\tilde{\mathbf{s}}_1$ or $\tilde{\mathbf{s}}_2$, represents a spectral distribution with N sampling points (dimensions), which is generated by a random set of current

composition.

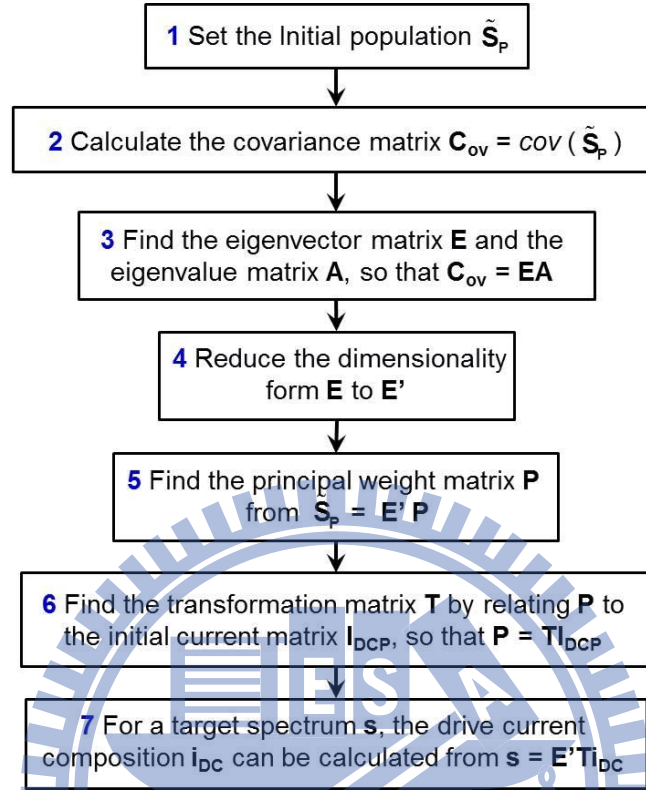


Figure 5-2 The schematic process of the reverse model.

2. It is useful to find out how much the dimensions vary from the mean with respect to each other by calculating the covariance matrix $C_{ov} = cov(\tilde{S}_p)$. The covariance matrix C_{ov} is a square matrix with n rows and columns. Each entry of the matrix represents the covariance between two individual dimensions. For example, the entry on row 2 and column 3, $C_{ov}(2, 3)$, can be given by:

$$C_{ov}(2, 3) = cov[\tilde{S}_p(2, :), \tilde{S}_p(3, :)] \quad (5-3)$$

Since $cov(a, b) = cov(b, a)$, the covariance matrix is symmetrical and the main diagonal are the variances of the dimensions themselves.

3. With the covariance matrix \mathbf{C}_{ov} , we can express the original data $\tilde{\mathbf{S}}_p$ in terms of a set of orthogonal axes; those are eigenvectors of the covariance matrix \mathbf{C}_{ov} . The \mathbf{C}_{ov} is therefore decomposed to the multiplication of the eigenvector matrix \mathbf{E} and eigenvalue matrix \mathbf{A} .

$$\mathbf{C}_{ov} = \mathbf{E}\mathbf{A} \quad (5-4)$$

4. The next step is to sort eigenvectors by their corresponding eigenvalues, which gives us the components (axes) in order of significance. The less important components can be ignored without losing much information. The selected principal components form a new matrix \mathbf{E}' with the reduced dimensionality.

5. The initial spectral population $\tilde{\mathbf{S}}_p$ now can be expressed as a linear combination of selected principal components, weighted by principal weights \mathbf{P} .

$$\tilde{\mathbf{S}}_p = \mathbf{E}'\mathbf{P} \quad (5-5)$$

where the weighting matrix is solved by the least square method

$$\mathbf{P} = (\mathbf{E}'^T\mathbf{E}')^{-1}\mathbf{E}'^T\tilde{\mathbf{S}}_p$$

6. The principal weight matrix \mathbf{P} is linearly related to the initial current matrix \mathbf{I}_{DCP} by a transformation matrix \mathbf{T} as:

$$\mathbf{P} = \mathbf{T}\mathbf{I}_{DCP} \quad (5-6)$$

where the transformation matrix can be obtained by using the pseudoinverse method $\mathbf{T} = \mathbf{P}\mathbf{I}_{DCP}^T(\mathbf{I}_{DCP}\mathbf{I}_{DCP}^T)^{-1}$.

7. Basically the linear relationship between the spectral distribution and the drive current has been established, by combining Equation (5-5) and (5-6). We simply express the relation as:

$$\tilde{\mathbf{s}} = \mathbf{R}\mathbf{i}_{\text{DC}}, \text{ where } \mathbf{R} = \mathbf{E}'\mathbf{T} \quad (5-7)$$

For a target spectrum \mathbf{s} , the drive current composition \mathbf{i}_{DC} can be immediately calculated by the same least square method $\mathbf{i}_{\text{DC}} = (\mathbf{R}^T\mathbf{R})^{-1}\mathbf{R}^T\mathbf{s}$.

5.2.3 Summary

In summary, we have made a step toward a better understanding of a computational theory of multispectral mixing for the spectral estimation problem, with the adaptation of the principal component analysis. The influences of the ignored components in step 4 as well as the projection errors produced from applying the least square method in step 5 and 7 should be further investigated. However, this iteration free model is indeed more efficient than the conventional optimization method, which has a great potential to be utilized in many photometric and radiometric applications.

Appendix

Color rendering index and color quality scale

A.1 The problems with *CRI*

The definition of color rendering index (*CRI*) from the International Commission on Illumination (CIE) is that: *CRI* is the “effect of an illuminant on the color appearance of objects by conscious or subconscious comparison with their color appearance under a reference illuminant.” In other words, by only a one-number output, *CRI*, we can assess the color rendering performance of light sources with respect to that of a standard light source, usually the daylight. To calculate *CRI*, we need to separately evaluate the appearance of fourteen color samples (Figure A-1) under the test light source and the reference source accordingly. If the resultant fourteen color points of the illuminated samples produced from the test light source are identical to those from the reference light source, the *CRI* is defined as 100. Table A-1 shows the *CRI* values for common lamps.



Figure A-1 *CRI* test color samples.

Table A-1 *CRI* values for common lamps ^[66].

Source	Color temperature	<i>CRI</i>
Candle	1700K	100
Low pressure Sodium	1700K	-47
High pressure Sodium	2100K	25
Domestic incandescent lamp	2700K	95 – 97
Tungsten Halogen	3200K	96 – 98
Fluorescent	2700K – 6500K	55 – 90
Metal Halide lamps	4000K – 7000K	60 – 95
Natural Sunlight	5000K – 6000K	100

However, *CRI* wasn't designed for evaluating the light sources with narrow spectral peaks, such as LEDs. For example, a RGB LEDs system still can get a respectable *CRI* even though the yellow region is a lack of the synthesized spectrum. The poor rendering of one or two colors will not significantly influence the score because the *CRI* is produced from the simple average of the rendering of all test samples. Furthermore, most of normally used sample colors (TCS01 to TCS08) are chosen to be mid-saturated, resulting in a misleading result for the sources used for the color rendition of deeply saturated colors. In recognition of these problems, the National Institute of Standards and Technology (NIST) has been developing a new metric named the Color Quality Scale (*CQS*).

A.2 Color Quality Scale

The *CQS*, like the *CRI*, is a test sample method, which employs a set of color samples all of higher chroma as shown in Figure A-2. The reason for the use of high saturated colors can be attributed to the important fact founded by NIST that, there is no light source spectrum that would render saturated colors well, while render unsaturated colors poorly ^[67]. On the other hand, the *CQS* adopts a more uniform CIELAB color space than that of the *CRI* used, and takes into account the observers preferences by reflecting the differences between hue and saturation shifts. Moreover, the refined mathematical treatment used to calculate *CQS* can avoid the shortcoming arose from the simple averaging of all color differences, as happens with *CRI*. That is, squaring each color difference before averaging them (root-mean-square) to ensure that the large rendering shift in any color sample can be adequately incorporated in the overall score.



Figure A-2 *CQS* test color samples.

Reference and links

- 1 E. F. Schubert, and J. K. Kim, "Solid-state light sources getting smart," *Science* **308**(5726), 1274–1278 (2005).
- 2 E. F. Schubert, J. K. Kim, H. Luo, and J.-Q. Xi "Solid-state lighting – A benevolent technology," *Rep Prog. Phys.* **69**, 3069-3098 (2006).
- 3 S. Pimputkar, J. S. Speck, S. P. DenBaars, and S. Nakamura, "Prospects for LED lighting," *Nat. Photonics* 3(4), 180–182 (2009).
- 4 J. K. Kim and E. F. Schubert, "Transcending the replacement paradigm of solid-state lighting," *Opt. Express* **16**, 21835–21842 (2008).
<http://www.opticsinfobase.org/oe/abstract.cfm?uri=oe-16-26-21835>
- 5 A. Žukauskas, R. Vaicekauskas, and M. S. Shur, "Solid-state lamps with optimized color saturation ability," *Opt. Express* **18**, 2287-2295 (2010).
- 6 A. Žukauskas, M. S. Shur, and R. Gaska, *Introduction to Solid-State Lighting* (Wiley, New York, 2002).
- 7 D. A. Steigerwald, J. C. Bhat, D. Collins, R. M. Fletcher, M. O. Holcomb, M. J. Ludowise, P. S. Martin, and S. L. Rudaz, "Illumination with solid state lighting technology," *IEEE J. Sel. Top. Quantum Electron.* **8**(2), 310–320 (2002).
- 8 M. Shur, and A. Žukauskas, "Solid-state lighting: Toward superior illumination," *Proc. IEEE* **93**(10), 1691–1703 (2005).
- 9 F. W. Billmeyer and M. Saltzman, *Principles of Color Technology*, 3rd edition (Wiley-Interscience, 2000).
- 10 E. F. Schubert, *Light Emitting Diodes*, 2nd edition (Cambridge University Press, 2006).
- 11 S. Chhajed, Y. Xi, Y. L. Li, T. Gessmann and E. F. Schubert, "Influence of junction temperature on chromaticity and color rendering properties of trichromatic white light source based on light emitting diodes," *J. Appl. Phys.* **97**, 054506 (2005).
- 12 A. Žukauskas, R. Vaicekauskas, and M. S. Shur, "Colour-rendition properties of solid-state lamps," *J. Appl. Phys.* **43**(35), 354006 (2010).
- 13 K. Müllen and U. Scherf, *Organic Light Emitting Devices. Synthesis, Properties and Applications*, 1st edition (Wiley-VCH, 2006).
- 14 A. Keppens, W. R. Ryckaert, G. Deconinck and P. Hanselaer, "Modeling high-power light-emitting diode spectra and their variation with junction temperature," *J. Appl. Phys.* **108**, 043104 (2010).
- 15 H. Y. Chou and T. H. Yang, "Dependence of emission spectra of LEDs upon junction temperature and driving current," *J. Light Visual Environ.* **32**, 183–186 (2008).
- 16 Y. Uchida, T. Taguchi, "Lighting theory and luminous characteristics of white

- light-emitting diodes,” *Opt. Eng.* **44**, 124003-1 (2005).
- 17 Y. Ohno, “Spectral design considerations for white LED color rendering,” *Opt. Eng.* **44**, 111302 (2005).
 - 18 F. Reifegerste and J. Lienig, “Modeling of the temperature and current dependence of LED spectra,” *J. Light Visual Environ.* **32**, 288–294 (2008).
 - 19 A. Žukauskas, R. Vaicekauskas, F. Ivanauskas, R. Gaska, and M. S. Shur, “Optimization of white polychromatic semiconductor lamps,” *Appl. Phys. Lett.* **80**(2), 234–236 (2002).
 - 20 K. Man, I. Ashdown, “Accurate colorimetric feedback for RGB LED clusters,” *SPIE* **6337**, 633702 (2006).
 - 21 Commission Internationale de l’Eclairage, “Colour rendering of white LED sources,” *Pub. CIE 177*, 2007.
 - 22 W. Davis, and Y. Ohno, “Toward and improved color rendering metrics,” *Proc. SPIE* **5941**, 59411G1–8 (2005).
 - 23 W. Davis and Y. Ohno, “Color quality scale,” *Opt. Eng.* **49**(10), 033602 (2010).
 - 24 M. S. Rea, and J. P. Freyssinier-Nova, “Color rendering: A tale of two metrics,” *Color Res. Appl.* **33**(3), 192–202 (2008).
 - 25 Y. Ohno, “Color rendering and luminous efficacy of white LED spectra,” *Proc. SPIE* **5530**, 88–98 (2004).
 - 26 A. Žukauskas, R. Vaicekauskas, F. Ivanauskas, H. Vaitkevičius, P. Vitta, and M. S. Shur, “Statistical approach to color quality of solid-state lamps,” *IEEE J. Sel. Top. Quantum Electron.* **15**(6), 1753–1762 (2009).
 - 27 G. He and L. Zheng, “Color temperature tunable white-light light-emitting diode clusters with high color rendering index,” *Appl. Opt.* **49**, 4670–4676 (2010).
 - 28 G. He and L. Zheng, “White-light LED clusters with high color rendering,” *Opt. Lett.* **35**, 2955–2957 (2010).
 - 29 I. Speier and M. Salsbury, “Color temperature tunable white light LED system,” *Proc. SPIE* **6337**, 63371F (2006).
 - 30 M. Born and E. Wolf, *Principle of Optics: Electromagnetic theory of propagation, Interference and Diffraction of light* (Cambridge University Press, Edinburg, 1999: 7th extended edition).
 - 31 C.-Y. Lee, A. Su, Y.-C. Liu, W.-Y. Fan, and W.-J. Hsieh, “In situ measurement of the junction temperature of light-emitting diodes using a flexible micro temperature sensor,” *Sensors* **9**, 5068–5075 (2009).
 - 32 Y. Xi and E.F. Schubert, “Junction-temperature measurement in GaN ultraviolet light-emitting diodes using diode forward voltage method,” *Appl. Phys. Lett.* **85**(12), 2163–2165 (2004).
 - 33 H.-Y. Ryu, K.-H. Ha, J.-H. Chae, O.-H. Nam, and Y.-J. Park, “Measurement of junction temperature in GaN-based laser diodes using voltage-temperature

- characteristics,” Appl. Phys. Lett. **87**, 093506 (2005).
- 34 Y. Xi, J.-Q. Xi, Th. Gessmann, J. M. Shah, J. K. Kim, E. F. Schubert, A. J. Fischer, M. H. Crawford, K. H. A. Bogart, and A. A. Allerman, “Junction and carrier temperature measurements in deep-ultraviolet light-emitting diodes using three different methods,” Appl. Phys. Lett. **86**, 031907 (2005).
 - 35 C. C. Lee and J. Park, “Temperature measurement of visible light-emitting diodes using nematic liquid crystal thermography with laser illumination,” IEEE Photo. Tech. Lett. **16**, 1706–1708 (2004).
 - 36 J. Park, M. Shin and C. C. Lee, “Measurement of temperature profiles on visible light-emitting diodes by use of a nematic liquid crystal and an infrared laser,” Opt.Lett. **29**, 2656–2658 (2004).
 - 37 N. Narendran, Y. Gu, and R. Hosseinzadeh, “Estimating junction temperature of high-flux white LEDs,” Proc. of SPIE **5366**, 158–160 (2004).
 - 38 Y. Gu, and N. Narendran, “A non-contact method for determining junction temperature of phosphor-converted white LEDs,” Proc. of SPIE **5187**, 107–114 (2004).
 - 39 TERCHY environmental technology Co. Taiwan, “HRMB-80 isothermal oven product catalog,” <http://www.terchy.com.tw/>.
 - 40 J. Hu, L. Yang, and M. W. Shin, “Electrical, optical and thermal degradation of high-power GaN/InGaN light-emitting diodes,” J. Phys. D: Appl. Phys. **41**, 035107 (2008).
 - 41 S. Chhajer, Y. Xi, Th. Gessmann, J.-Q. Xi, J. M. Shah, J. K. Kim, and E. F. Schubert, “Junction temperature in light-emitting diodes assessed by different methods,” Proc. SPIE, **5739**, 16–25 (2005).
 - 42 N. C. Chen, Y. K. Yang, W. C. Lien, and C. Y. Tseng, “Forward current-voltage characteristics of an AlGaInP light-emitting diode,” J. Appl. Phys. **102**, 043706 (2007).
 - 43 J. Chonko for Keithley Instruments Inc., “Using Forward Voltage to Measure Semiconductor Junction Temperature,” Application Note (2006).
 - 44 A. Keppens, “Modelling and evaluation of high-power light-emitting diodes for general lighting,” Ph.D. Thesis, Catholic University College Gent (2010).
 - 45 W. J. Smith, *Modern optical engineering*, third edition (McGraw-Hill Professional, 2000).
 - 46 R. Kingslake, *Lens design fundamentals* (Academic Press, 1978).
 - 47 Epistar Corporation, Taiwan, General LED product catalog (2010).
 - 48 Toyoda Gosei Corporation, Japan, LED product catalog (2010).
 - 49 J. J. McCann, S. P. McKee, and T. H. Taylor, “Quantitative studies in retinex theory. A comparison between theoretical predictions and observer responses to the “color mondrian” experiments,” Vision Res. **16**(5), 445–458 (1976).

- 50 R. Mirhosseini, M. F. Schubert, S. Chhajed, J. Cho, J. K. Kim, and E. F. Schubert, "Improved color rendering and luminous efficacy in phosphor-converted white light-emitting diodes by use of dual-blue emitting active regions," *Opt. Express* **17**, 10806–10813 (2009). <http://www.opticsinfobase.org/abstract.cfm?URI=oe-17-13-10806>.
- 51 A. R. Duggal, "Organic electroluminescent devices for solid state lighting," *Electroluminescence*, Z. H. Kafafi (Taylor & Francis Group, Boca Raton, Florida, 2005).
- 52 N. Ohta and A. Robertson, *Colorimetry: Fundamentals and Applications* (Wiley-Blackwell, 2005).
- 53 R. L. Haupt, and S. E. Haupt, *Practical Genetic Algorithms*, 2nd edition (John Wiley, 2004).
- 54 W. J. Smith, *Modern Lens Design*, Second edition (McGraw-Hill, 2005).
- 55 M. Laikin, *Lens Design*, Fourth edition (CRC Press, 2006).
- 56 I. Moreno, M. Avendaño-Alejo, and R. I. Tzonchev, "Designing light-emitting diode arrays for uniform near-field irradiance," *Appl. Opt.* **45**, 2265–2272 (2006).
- 57 R. S. Berns, "A genetic approach to color modeling," *Color Res. Appl.* **22**, 318–325 (1997).
- 58 T. Mukai, M. Yamada and S. Nakamura, "Characteristics of InGaN-Based UV/Blue/Green/Amber/Red Light-Emitting Diodes," *Jpn. J. Appl. Phys.* **38**, 3976–3981 (1999).
- 59 Philips Lumileds Lighting Campany, Netherlands, LUXEON Rebel PC Amber Datasheet DS62 (2010).
- 60 T. Treurniet and V. Lammens, "Thermal management in color variable multi-chip LED modules," 22nd IEEE SEMI-THERM Symposium (2006).
- 61 L. Kim, J. Choi, S. Jang, and M. W. Shin, "Thermal analysis of multi-chip LED packages," *Proc. of SPIE* **6355**, 63550 (2006).
- 62 I. Fryc, S. W. Brown, G. P. Eppeldauer, and Y. Ohno, "LED-based spectrally tunable source for radiometric, photometric, and colorimetric applications," *Opt. Eng.* **44**, 111309 (2005).
- 63 S. W. Brown and B. C. Johnson, "Advances in radiometry for ocean color," *Proc. of SPIE* **5151**, 441 (2003).
- 64 I. Fryc and E. Czech, "Spectral correction of the measurement CCD array," *Opt. Eng.* **41**(10), 2402–2406 (2002).
- 65 I. T. Jolliffe, *Principal Component Analysis*, Second edition (Springer, 2002).
- 66 M. Wood, "CRI-what does it really mean?" *Protocol Winter* **15**(1), 14–18 (2010).
- 67 M. Wood, "CRI and the Color Quality Scale, Part 2" *Protocol Spring* **15**(2), 14–18 (2010).

Publication List

Journal Papers

1. **Ming-Chin Chien** and Chung-Hao Tien, “Multispectral mixing scheme for LED clusters with extended operational temperature window,” *Opt. Express* **20**, A245-A254 (2012).
2. **Ming-Chin Chien** and Chung-Hao Tien, “Cluster LEDs mixing optimization by lens design techniques,” *Opt. Express* **19**, A804-A817 (2011).
3. **Ming-Chin Chien**, Yu Lung Tung, and Chung-Hao Tien, “Ultracompact backlight -reversed concentration optics,” *Appl. Opt.* **48**, 4142-4148 (2009).

International Conference Papers

1. **Ming-Chin Chien** and Chung-Hao Tien, “Multispectral Optimization for Cluster LEDs with Wide Operable Range,” SID12 19.3, Boston, USA (2012).
2. **Ming-Chin Chien** and Chung-Hao Tien, “Cluster LED Spectral Optimization as Lens Design,” SID11 54.3, Los Angeles, USA (2011).
3. **Ming-Chin Chien**, Hsiao-Ju Chen, Yu-Lung Tung and Chung-Hao Tien, “Optimal Additive Mixing Approach via Multi-Color LEDs Platform,” SID10 68.4, Seattle, USA (2010).
4. **Ming-Chin Chien**, Chih-Hong Lin, and Chung-Hao Tien, “Backlight Type Daylight Concentrator,” ICAM10 162, Kenting, Taiwan (2010).
5. **Ming-Chin Chien**, Cho-Chih Chen, Yen-Hsing Lu, Hao-Chung Kuo, Chung-Hao Tien and Su-Chin Yang, “LED Light Lit for Field-Sequential-Color Backlight System,” AD50182, Shanghai, China (2007).
6. **Ming-Chin Chien**, Chung-Hao Tien, Cho-Chih Chen and Yen-Hsing Lu, “Region-Partitioned LED Backlight Design for Field Sequential Color LCD,” SID07 P-67, Long Beach, USA (2007).

Patent pending

1. Yu Shu Chen, **Ming-Chin Chien**, Chih Ming Lai, “ILLUMINATION APPARATUS,” Taiwan Patent Number : 201122363
2. **Ming-Chin Chien**, An Chi Wei, Jyh Long Chern, Wen Jang Jiang, “REFLECTIVE COVER AND ILLUMINATION DEVICE,” Taiwan Patent Number : 201107670
3. Pei Yuan Hung, **Ming-Chin Chien**, Yu Shu Chen, Chih Ming Lai, “REFLECTING COVER AND ILLUMINATION DEVICE,” Taiwan Patent Number : 201107671
4. **Ming-Chin Chien**, Wen Shsin Sun, “OPTICAL READING/RECORDING SYSTEM,” Taiwan Patent Number : 200903472
5. Hsuen Chen Chang, **Ming-Chin Chien**, Shsn Ju Lin, “HEAT DISSIPATION DEVICE,” Taiwan Patent Number : D134439

Awards

- International Conference on Advanced Manufacture (ICAM) 2010 Best Paper Award.
- Optical Photonics Taiwan (OPT) 2006 Best Student Award.
- 96 學年度國立交通大學光電工程系博士生入學獎學金。



Vita

Name: Ming-Chin Chien 簡銘進

Day of birth: Oct. 28 1981

Address: 基隆市安樂路 2 段 166 巷 40-5 號

Education

Sep. 07' – Jun. 12' : National Chiao Tung University, Hsinchu, Taiwan.

PhD in Institute of Electro-Optical Engineering

Sep. 04' – Jun. 07' : National Chiao Tung University, Hsinchu, Taiwan.

M.S. in Display Institute

Sep. 00' – Jun. 04' : National Chung Cheng University, Chiayi, Taiwan

B.S. in Physics

Experience

Apr. 10' – Oct. 10' : Visiting scholar at the Technische Universitat
Ilmenau, Germany.

Aug. 08' – Dec. 08' : Short-term practical training at the Foxsemicon
Integrated technology Inc.